



University of Kentucky
UKnowledge

University of Kentucky Master's Theses

Graduate School

2010

CHARACTERIZATION OF DEFECTS IN METAL SHEETS VIA INFRARED THERMOGRAPHY

Marc Anthony Harik
University of Kentucky, marcharik@gmail.com

[Right click to open a feedback form in a new tab to let us know how this document benefits you.](#)

Recommended Citation

Harik, Marc Anthony, "CHARACTERIZATION OF DEFECTS IN METAL SHEETS VIA INFRARED THERMOGRAPHY" (2010). *University of Kentucky Master's Theses*. 32.
https://uknowledge.uky.edu/gradschool_theses/32

This Thesis is brought to you for free and open access by the Graduate School at UKnowledge. It has been accepted for inclusion in University of Kentucky Master's Theses by an authorized administrator of UKnowledge. For more information, please contact UKnowledge@lsv.uky.edu.

ABSTRACT OF THESIS

CHARACTERIZATION OF DEFECTS IN METAL SHEETS VIA INFRARED THERMOGRAPHY

Defects in Aluminum, Stainless steel and galvanized steel sheets are studied in reflection mode infrared thermography. The effect of material properties, surface finish, heating intensity, heater emission spectra, pixel size and defect size are studied. Contrast is governed by heat quality, emissivity and defect geometry—which follows a logarithmic trend. The diameter detected via infrared thermography is found to be at least 30% larger than the measured diameter and sub-pixel defects can be detected. The use of gradient and Laplacian of temperature is introduced as a means of increasing defect contrast and mitigating heater variation.

KEYWORDS: Infrared Thermography, Non-destructive Testing, Non-destructive Examination, Inspection, Manufacturing

Marc Harik

December 7, 2010

CHARACTERIZATION OF DEFECTS IN METAL SHEETS VIA INFRARED THERMOGRAPHY

By

Marc Anthony Harik

Kozo Saito

Director of Thesis

James M. McDonough

Director of Graduate Studies

THESIS

Marc Anthony Harik

The Graduate School

University of Kentucky

2010

CHARACTERIZATION OF DEFECTS IN METAL SHEETS VIA INFRARED THERMOGRAPHY

THESIS

A thesis submitted in partial fulfillment of the requirements
for the degree of Master of Science in Mechanical Engineering in the
College of Engineering at the
University of Kentucky

By

Marc Anthony Harik
Lexington, Kentucky

Director: Dr. Kozo Saito, Professor of Mechanical Engineering

Lexington, Kentucky

2010

Copyright © Marc A. Harik 2010

Dedicated to those who came before and those who come next.

ACKNOWLEDGEMENTS

No work is a truly individual endeavor. Everything is an accumulation of experiences with people that shape who we are and influence our work. I thank my family and friends for their support throughout my life and academic career. I would also like to thank all of my co-workers at the institute of research for technology development.

I am extremely thankful to Dr. Kozo Saito, for his support throughout my undergraduate and graduate studies. The unique mix of people Dr. Saito has brought together has been a great help in my growth as a researcher, engineer and as a person. My committee members Drs. Abraham Salazar and Tianxiang Li, for their expertise and criticism on this thesis and other research projects I have assisted with.

I am very grateful to Dr. Belal Gharaibeh and Ahmad Salaimeh for their invaluable guidance, assistance and friendship through my time at the institute of research for technology development. A special thanks Herbert Mefford, for machining the samples and putting up with my oftentimes ridiculous questions. Lastly I would like to thank the many professors and graduate students I have worked and studied with.

TABLE OF CONTENTS

ACKNOWLEDGEMENTS.....	iii
LIST OF TABLES.....	vi
LIST OF FIGURES.....	vii
Chapter One: Introduction.....	1
i. Review of Nondestructive Technology	1
ii. Background	3
Chapter Two: Experimental Methods.....	5
i. Mathematical Formulation	5
ii. Apparatus	12
Detector	12
Heaters.....	13
iii. Sample Preparation.....	16
iv. Estimation of Uncertainty	20
v. Experimental Procedure.....	21
Chapter Three: Results and Discussion.....	22
i. Sample Images	23
ii. Effect of Diameter	28
iii. Detected Diameter.....	31
iv. Effect of Aspect Ratio	34
v. Apparent Emissivity.....	35

vi. Effect of Heating and Heaters	37
vii. Derivatives as Filters.....	39
Chapter Four: Conclusions and Future Work.....	43
Appendix A: Defect Sizes	45
References	49
Vita	51

LIST OF TABLES

Table 2.1 Heater settings for the black body and ceramic heater; controlled parameters are in bold.	15
Table 2.2 Thermal properties of materials studied.	16
Table 2.3 The nominal depth and diameter for each defect plate.	17
Table A.1 Defect Measurements for Aluminum Mirror-Like Finish Samples.	45
Table A.2 Defect Measurements for Aluminum Satin Finish Samples.	46
Table A.3 Defect Measurements for Steel Mirror-Like Finish Samples.	47
Table A.4 Defect Measurements for Steel Unpolished Finish Samples.	47
Table A.5 Defect Measurements for Galvanized Steel Samples.	48

LIST OF FIGURES

Figure 1-1 Reflection and transmission mode schematics.	3
Figure 2-1 Energy balance diagram for a grey body	5
Figure 2-2 Schematic of Experimental Setup.....	12
Figure 2-3 Infrared Salamander Half Trough Emitter Schematic [34].....	14
Figure 2-4 The defect plate arrangement.....	17
Figure 2-5 Circle Fitted to points chosen along the edge of the defect.	18
Figure 2-6 a) Microscopic image of defect in mirror finish steel sheet b) Processed black and white image c) Processed image with surroundings removed and holes filled in d) Errant pixels removed and morphological operations performed.	19
Figure 3-1 Array 3 of mirror-like finish Aluminum with a) black body heater at 373 K b) ceramic heater at 1093 W/m ²	23
Figure 3-2 Array 3 of satin finish Aluminum with a) black body heater at 473 K b) ceramic heater at 1093 W/m ²	24
Figure 3-3 Array 2 of mirror-like finish stainless steel with a) black body heater at 303 K b) ceramic heater at 478 W/m ²	25
Figure 3-4 Array 3 of unpolished stainless steel with a) black body heater at 323 K b) ceramic heater at 615 W/m ²	26
Figure 3-5 Temperature maps of Array 3 of galvanized steel with a) black body heater at 573 K b) ceramic heater at 6831 W/m ²	27
Figure 3-6 Diameter divided by pixel size plotted against contrast for array 3 with the black body heater at 373 K.....	28
Figure 3-7 Effect of diameter for the array 3 with the black body heater at 373 K a) Low emissivity samples b) High emissivity samples.	29

Figure 3-8 Contrast of a defect with D/px of 6.	30
Figure 3-9 Detected diameter divided by the measured diameter plotted against the measured diameter over pixel size. Ceramic heater set to 478 W/m^2	31
Figure 3-10 Detected diameter divided by the measured diameter plotted against the measured diameter over pixel size. Black body heater set to 573 K	32
Figure 3-11 Measured diameter divided by the detected diameter and plotted against the measured diameter over pixel size for all array 3 tests.	33
Figure 3-12 The effect of aspect ratio on contrast using data from array 1 with the black body heater at 373 K	34
Figure 3-13 Apparent emissivity of a cavity opening for a cylindrical cavity of finite length with diffuse reflecting walls at a constant temperature. From Robert Siegel, John R. Howell; <i>Thermal Radiation Heat transfer</i> , 4th Edition [37].	35
Figure 3-14 Apparent emissivity for the array 1 defects in the aluminum samples.	36
Figure 3-15 The effect of heating temperature on contrast by heater type on Aluminum samples with $D \approx 2\text{mm}$	37
Figure 3-16 Effect of heat quality on contrast with respect to heater type.	38
Figure 3-17 Aluminum Mirror Array 3 with ceramic heater at 2732 W/m^2 a) thermogram b) magnitude of the gradient of the thermogram c) Laplacian of the thermogram.	40
Figure 3-18 Contrast maps for a) gradient of temperature b) Laplacian of temperature.	41
Figure 3-19 Average contrast by material for all defects, heating conditions and arrays.	42

Chapter One: Introduction

i. Review of Nondestructive Technology

Nondestructive testing is often an essential step in ensuring product quality economically as safety factors are reduced and the demand on machines increases. Testing nondestructively transitioned from a laboratory operation to a valuable production tool in the 1920's [1]. The man-power shortage caused by the First World War, demonstrated the need for automated and fool-proof methods of inspection that did not rely on operator judgment [2]. To reduce defects, an inspection must provide feedback to processes upstream when a defect is discovered; increasing the number of off-line post-mortem judgment inspections can only increase the reliability of inspection [3].

Manual visual inspection is one of the easiest forms of inspection to implement and is the most common [4], but it is not necessarily the most reliable or cost-effective. Machine assisted vision systems may aid inspectors—however, they are subjective, require highly trained personal and relatively slow production speeds [5]. Automated mechanical-optical systems, eddy current detection, ultrasonic testing and infrared thermography all seek to provide more reliable inspection methods and detect a wide range of defects.

Automated optical inspection systems are fast and can inspect as large area, but they cannot detect subsurface defects in metal sheets [6-8]. Eddy current detection is fast and can detect micron scale defects on the surface and in-depth, but the scanning area is relatively small, and is used in the aircraft and space industry [5, 9, 10]. Ultrasonic inspection and acoustic emissions can be used to determine grains size, inspect welds and determine elasticity, but requires contact and in the case of metal sheets, a large sample [11-13]. Infrared thermography

can be implemented on line in both active and passive sensing modes. It has been used to detect defects in the steel making process, marine coatings [14] and painted surfaces in automotive applications [15].

“Quality can be assured reasonable only when it is built in at the process and when inspection provides immediate and accurate feedback at the source of defects.” -Shigeo Shingo [3]. In reaching this goal, infrared thermography allows for high speed inspection surface and sub-surface inspection of large areas and may be useful in determining root cause.

ii. Background

The infrared spectrum is normally split into three different ranges for inspection; short or near wave (.75–3 μm), middle wave (3–6 μm) and long or far (8–15 μm) [4, 16]. There are two main types of thermal sensors used in focal plane arrays, photonic and micro-bolometer. Micro-bolometers are sensitive over a wide range but have a longer response time than photonic detectors [4]. Photonic detectors have a very fast response time with a limited spectral response and usually require cooling [4, 16].

Infrared sensing is either passive or active. In the active mode, the sample is heated or stimulated for the purposes of inspection. In passive mode, the emissions from the sample and reflections from its surroundings are studied without a stimulus provided for the purpose of inspection [1]. Active sensing can generally be performed in either reflection or transmission or reflection mode as shown in Figure 1-1.

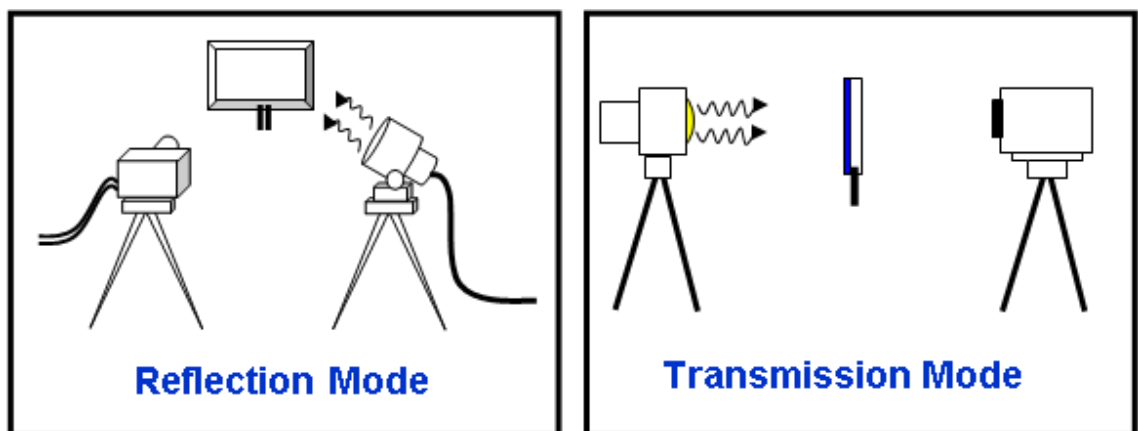


Figure 1-1 Reflection and transmission mode schematics.

Reflection mode thermography may be used to detect surface and subsurface defects, where transmission mode may detect defect throughout the sample. Reflection mode thermography is not ideal for cases with a high rate of transmission—for instance

most plastics at low power intensities [17]. In some cases heating may be applied to the sample volumetrically with eddy currents

Infrared thermography has been used to inspect carbon fiber [18-22], steel [23, 24], ceramics [25, 26], coatings [14], concrete [27, 28] and in medical applications [29]. This thesis seeks to characterize defects in metal sheets via infrared thermography via scaling laws.

Chapter Two: Experimental Methods

i. Mathematical Formulation

A body subjected to incident radiation will reflect, absorb and transmit the incoming energy to various degrees depending on its material properties. For an opaque grey body the incident energy will be absorbed and reflected depending on the properties of the material's surface as described in Equation 2.1.

$$E_{incident} = E_{reflected} + E_{absorbed} \quad (2.1)$$

The absorbed energy will be lost to the environment in forms of convection from the surface, radiation to the surroundings and conduction within the body as shown in Figure 2-1.

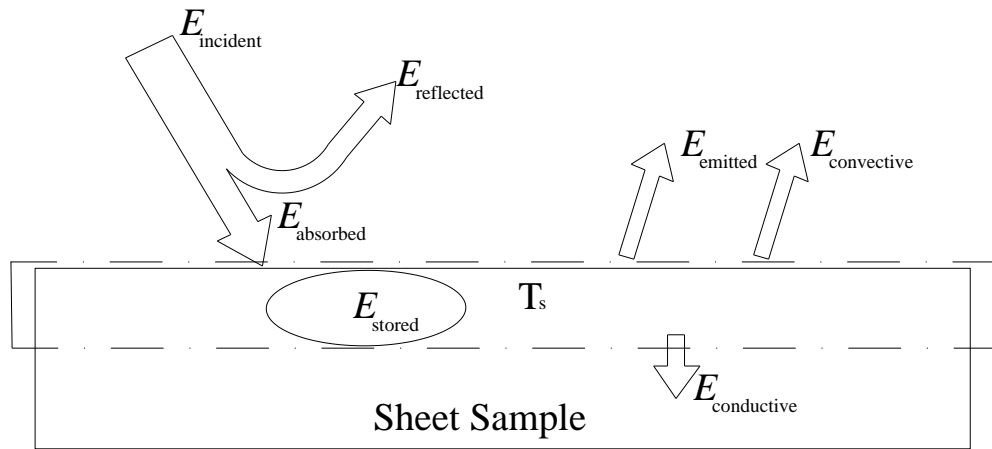


Figure 2-1 Energy balance diagram for a grey body

Performing an energy balance for the grey body, the amount of energy absorbed is equal to the energy stored, conducted through the body, emitted and lost to convection.

$$E_{absorbed} = E_{conductive} + E_{stored} + E_{convective} + E_{emitted, T_{\infty}} \quad (2.2)$$

Substituting in equations in for each term in Equation 2.2

$$E_{absorbed} = lA_{px}\nabla(k \cdot \nabla T) + lA_{px}\frac{k}{\alpha}\frac{\partial T_s}{\partial t} + hA_{px}(T_s - T_\infty) + \int_0^\infty \int_0^{4\pi} \varepsilon_s \sigma A_{px} F_{px-\infty} (T_s^4 - T_\infty^4) \partial\omega \partial\lambda \quad (2.3)$$

A_{px} , l and $F_{px-\infty}$ are the pixel area, thickness of the material and the view factor of one pixel to infinity respectively. The energy imparted unto the infrared detector for each pixel, E_d , is a combination of the energy reflected and emitted from the grey body as well as radiation from the surroundings as described in Equation 2.4.

$$E_d = F_{px-d}(E_{reflected} + E_{emitted,T_d} + C) \quad (2.4)$$

C is a constant and includes the radiation from the surroundings and machine error. Solving Equation 2.1 for the energy reflected.

$$E_{reflected} = E_{incident} - E_{absorbed} \quad (2.5)$$

Substituting Equation 2.5 into Equation 2.4 to describe the energy reaching the detector in terms of the incident, absorbed and emitted energy:

$$E_d = F_{px-d}(E_{incident} - E_{absorbed} + E_{emitted} + C) \quad (2.6)$$

Substituting Equation 2.3 into Equation 2.6:

$$\begin{aligned}
E_d = F_{px-d} & \left(E_{incident} - lA_{px} \nabla(k \cdot \nabla T) - lA_{px} \frac{k}{\alpha} \frac{\partial T_s}{\partial t} - hA_{px}(T_s - T_\infty) \right. \\
& - \int_0^\infty \int_0^{4\pi} \varepsilon_s \sigma A_{px} F_{px-\infty} (T_s^4 - T_\infty^4) \partial\omega \partial\lambda \\
& \left. + \int_0^\infty \int_0^{4\pi} \varepsilon_s A_{px} \sigma (T_s^4 - T_d^4) \partial\omega \partial\lambda + C \right)
\end{aligned} \tag{2.7}$$

The incident radiation is affected by the view factor of the pixel to the heater (F_{px-H}), the area of the pixel (A_{px}) and the energy emitted from the heater (E_H). Note the energy emitted from the heater is determined a priori. The energy emitted from the heater is assumed to be much greater than that of the surroundings.

$$E_{incident} = A_{px} F_{px-H} E_H \tag{2.8}$$

Substituting the incident energy from Equation 2.8 into Equation 2.7 produces Equation 2.9.

$$\begin{aligned}
E_d = F_{px-d} & \left(A_{px} F_{px-H} E_H - lA_{px} \nabla(k \cdot \nabla T) - lA_{px} \frac{k}{\alpha} \frac{\partial T_s}{\partial t} - hA_{px}(T_s - T_\infty) \right. \\
& - \int_0^\infty \int_0^{4\pi} \varepsilon_s \sigma A_{px} F_{px-\infty} (T_s^4 - T_\infty^4) \partial\omega \partial\lambda \\
& \left. + \int_0^\infty \int_0^{4\pi} \varepsilon_s A_{px} \sigma (T_s^4 - T_d^4) \partial\omega \partial\lambda + C \right)
\end{aligned} \tag{2.9}$$

Factoring out the area of a pixel, assuming it is constant.

$$\begin{aligned}
E_d = A_{px} F_{px-d} & \left(F_{px-H} E_H - l \nabla(k \cdot \nabla T) - l \frac{k}{\alpha} \frac{\partial T_s}{\partial t} - h(T_s - T_\infty) \right. \\
& - \int_0^\infty \int_0^{4\pi} \varepsilon_s \sigma F_{px-\infty} (T_s^4 - T_\infty^4) \partial\omega \partial\lambda \\
& \left. + \int_0^\infty \int_0^{4\pi} \varepsilon_s \sigma (T_s^4 - T_d^4) \partial\omega \partial\lambda + C_2 \right)
\end{aligned} \tag{2.10}$$

For a steady state condition with $T_s \approx T_\infty$, Equation 2.10 can be simplified as there is no longer storage, convection or emission to the surroundings.

$$E_d = A_{px} F_{px-d} \left(F_{px-H} E_H - l \nabla(k \cdot \nabla T) + \int_0^\infty \int_0^{4\pi} \varepsilon_s \sigma (T_s^4 - T_d^4) \partial\omega \partial\lambda + C_2 \right) \quad (2.11)$$

Taking the gradient in x, y and z of the detector energy:

$$\begin{aligned} \nabla E_d = A_{px} \nabla F_{px-d} & \left(F_{px-H} E_H - l \nabla(k \cdot \nabla T) + \int_0^\infty \int_0^{4\pi} \varepsilon_s \sigma (T_s^4 - T_d^4) \partial\omega \partial\lambda \right. \\ & \left. + C \right) \\ & + A_{px} F_{px-d} \left[\nabla(F_{px-H} E_H) - \nabla(l \nabla(k \cdot \nabla T)) \right. \\ & \left. + \nabla \int_0^\infty \int_0^{4\pi} \varepsilon_s \sigma (T_s^4 - T_d^4) \partial\omega \partial\lambda \right] \end{aligned} \quad (2.12)$$

Assuming the energy from the heater is uniform.

$$\begin{aligned} \nabla E_d = \frac{\nabla F_{px-d}}{F_{px-d}} E_d \\ + A_{px} F_{px-d} \left[E_H \nabla F_{px-H} - \nabla(l \nabla(k \cdot \nabla T)) \right. \\ \left. + \nabla \int_0^\infty \int_0^{4\pi} \varepsilon_s \sigma (T_s^4 - T_d^4) \partial\omega \partial\lambda \right] \end{aligned} \quad (2.13)$$

Taking the Laplacian of the detector energy:

$$\begin{aligned}
\nabla^2 E_d &= \frac{F_{px-d} \nabla^2 F_{px-d} - \nabla F_{px-d}^2}{F_{px-d}^2} E_d + \frac{\nabla F_{px-d}}{F_{px-d}} \nabla E_d \\
&+ A_{px} \nabla F_{px-d} \left[E_H \nabla F_{px-H} - \nabla(l \nabla(k \cdot \nabla T)) \right. \\
&+ \left. \nabla \int_0^\infty \int_0^{4\pi} \varepsilon_s \sigma (T_s^4 - T_d^4) \partial \omega \partial \lambda \right] \\
&+ A_{px} F_{px-d} \left[E_H \nabla^2 F_{px-H} - \nabla^2(l \nabla(k \cdot \nabla T)) \right. \\
&+ \left. \nabla^2 \int_0^\infty \int_0^{4\pi} \varepsilon_s \sigma (T_s^4 - T_d^4) \partial \omega \partial \lambda \right]
\end{aligned} \tag{2.14}$$

Substituting in the value for the gradient in Equation 2.13 and simplifying.

$$\begin{aligned}
\nabla^2 E_d &= \frac{\nabla^2 F_{px-d}}{F_{px-d}} E_d \\
&+ 2A_{px} \nabla F_{px-d} \left[E_H \nabla F_{px-H} - \nabla(l \nabla(k \cdot \nabla T)) \right. \\
&+ \left. \nabla \int_0^\infty \int_0^{4\pi} \varepsilon_s \sigma (T_s^4 - T_d^4) \partial \omega \partial \lambda \right] \\
&+ A_{px} F_{px-d} \left[E_H \nabla^2 F_{px-H} - \nabla^2(l \nabla(k \cdot \nabla T)) \right. \\
&+ \left. \nabla^2 \int_0^\infty \int_0^{4\pi} \varepsilon_s \sigma (T_s^4 - T_d^4) \partial \omega \partial \lambda \right]
\end{aligned} \tag{2.15}$$

For a defect free isentropic metal sheet of uniform thickness, constant material properties and surface roughness l , k and ε_s are constant.

$$\begin{aligned}
\nabla^2 E_d = & \frac{\nabla^2 F_{px-d}}{F_{px-d}} E_d \\
& + 2A_{px} \nabla F_{px-d} \left[E_H \nabla F_{px-H} - lk \nabla^3 T \right. \\
& + \left. \int_0^\infty \int_0^{4\pi} \varepsilon_s \sigma \nabla (T_s^4 - T_d^4) \partial \omega \partial \lambda \right] \\
& + A_{px} F_{px-d} \left[E_H \nabla^2 F_{px-H} - lk \nabla^4 T \right. \\
& + \left. \int_0^\infty \int_0^{4\pi} \varepsilon_s \sigma \nabla^2 (T_s^4 - T_d^4) \partial \omega \partial \lambda \right]
\end{aligned} \tag{2.16}$$

Assuming the temperature of the detector is constant with respect to position and that the view factor of each pixel to the heater and to the detector is approximately constant in the neighborhood of a pixel.

$$\nabla^2 E_d = A_{px} F_{px-d} \left(-lk \nabla^4 T + \int_0^\infty \int_0^{4\pi} \varepsilon_s \sigma \nabla^2 T_s^4 \partial \omega \partial \lambda \right) \tag{2.17}$$

For metal sheets with a Biot number $\ll .1$ the temperature of the sheet can be assumed constant.

$$\nabla E_d \approx 0 \text{ and } \nabla^2 E_d \approx 0 \tag{2.18}$$

The temperature of each pixel is correlated to the radiation sensed by the detector over its detection band.

$$T_m = \int_{\lambda_{D,l}}^{\lambda_{D,h}} \int_0^{4\pi} E_d \partial \omega \partial \lambda \tag{2.19}$$

Where $\lambda_{D,h}$ and $\lambda_{D,l}$ are the maximum wavelength and minimum wavelength the detector is sensitive to. Thus $\nabla T_m \approx 0$ and $\nabla^2 T_m \approx 0$ if $\nabla E_d \approx 0$ and $\nabla^2 E_d \approx 0$ respectively. The

parameters that influence the temperature measurement for cylindrical defects are listed in Equation 2.20.

$$T_m = f(k, \rho, C, \varepsilon_s, T_\infty, T_s, Q_H, T_H, A_{px}, D, l) \quad (2.20)$$

ii. Apparatus

Samples were inspected in reflection mode infrared thermography. Since specular or partial specular reflection is expected with the samples, the infrared detector and heater are positioned at opposite but equal angles to the sample surface's normal as shown in Figure 2-2.

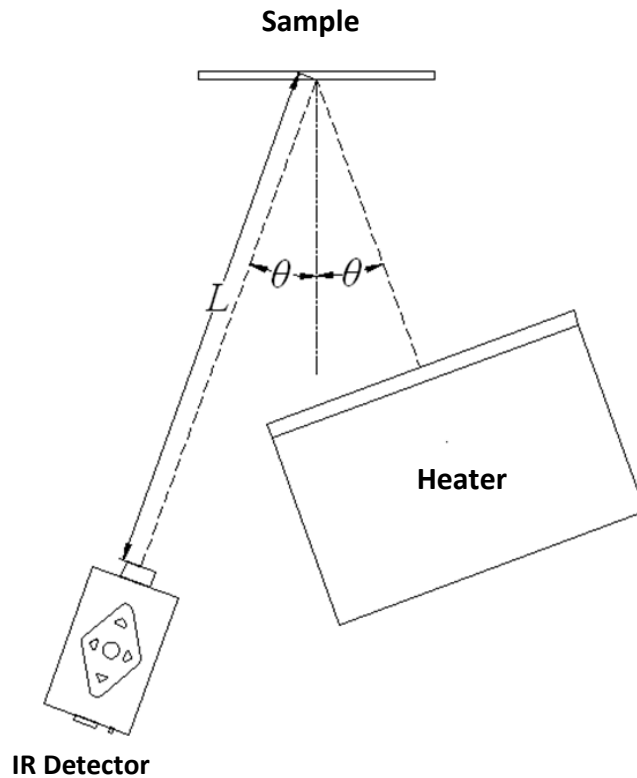


Figure 2-2 Schematic of Experimental Setup

Detector

Two FLIR ThermoVision SC4000 photonic—made from Indium Antimonide—mid-wave infrared (MWIR) detectors were used for this experiment. The ThermoVision SC4000 MWIR has a spectral range of 3 μm to 5 μm with a pixel pitch of 30 μm x 30 μm and a sensitivity of 0.025 $^{\circ}\text{C}$ [30]. The cameras were equipped with a 25 mm and 50 mm focal length lenses and were

positioned 31 cm and 54 cm away from the sample to produce a spot or pixel (px) size of .375 mm and .325 mm respectively. The SC4000 with the 25 mm lens was used for heater settings less than or equal to 100 °C, while the SC4000 with the 50 mm lens was used for heater temperatures greater than 100 °C.

Heaters

The Infrared Systems Development IR-160 black body with an IR-301 temperature controller was selected as it is a nearly uniform heater with black body emission characteristics. The heating portion of the IR-160 is 12" (30.5 cm) square and has a surface temperature that varies less than ± 0.1 °C spatially and temporally (for a short term) with an emissivity of $0.96 \pm 0.02\%$ [31, 32].

Two 500W Infrared Salamander ceramic heaters were chosen as the emission spectrum of ceramics ranges from 2 μm to 10 μm peaking at 5 μm [25, 33]. Each heater draws a maximum of 500W at 120V and is controlled by a potentiometer. Total wattage used was measured by a Kill-A-Watt P4400 which is accurate to $\pm 0.1\text{W}$ was placed before the potentiometer. The dimensions of the heater as provided by the manufacturer are shown in Figure 2-3.

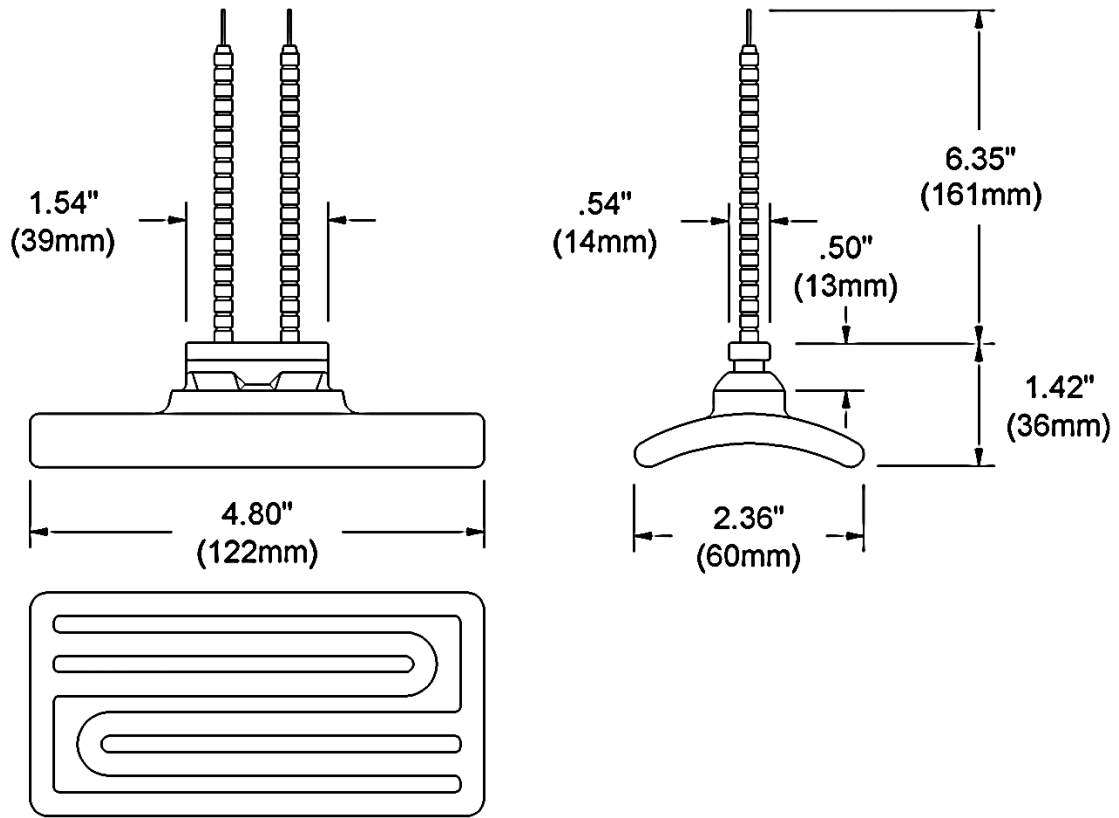


Figure 2-3 Infrared Salamander Half Trough Emitter Schematic [34].

The overall view factor to the sample to the blackbody heater is .19 and .035 for the IR ceramic heater. The view factors were calculated using the contour double integral formula (CDIF) while assuming both were planar surfaces[35, 36]. The IR-160 was operated from 303 K to 573 K while the Ceramic Heater was operated with a heat flux between 480 W/m² to 6800 W/m². To compare the two heaters, the heat quality—the amount of exergy destroyed— was considered. For this case as there is no work or chemical exergy to consider.

$$HQ = Q_h \left(1 - \frac{T_c}{T_h} \right)$$

Where T_c is the ambient temperature, T_h is the heater temperature and Q_h is the heat emitted from the heater. Settings were chosen such that the heat output from both heaters matches as shown Table 2.1 lists the different heater settings used.

Table 2.1 Heater settings for the black body and ceramic heater; controlled parameters are in bold.

Black Body			Ceramic Heater		
Q_h [W/m ²]	T [K]	HQ [W/m ²]	Q_h [W/m ²]	T [K]	HQ [W/m ²]
479	303	8	478	313	8
618	323	48	615	318	47
1099	373	221	1093	332	218
2842	473	1051	2732	389	994
6119	573	2936	6831	488	3374
			10245	538	4665

iii. Sample Preparation

Sheets of Aluminum alloy 5052, stainless steel type 304 and Galvanized steel ASTM A653 (Carbon Steel type B hot dipped in Zinc finish) were chosen with thicknesses of 1.9mm to 2.0mm. Two finishes were tested for the Aluminum and stainless steel sheets. The Aluminum sheet was selected in a mirror-like No. 8 finish and a Satin No. 4 finish, while the stainless steel was selected in a mirror-like No. 8 finish and an unpolished finish. Thermal properties from literature are listed in Table 2.2 [4, 37, 38].

Table 2.2 Thermal properties of materials studied.

Material	Thermal Conductivity	Density	Specific Heat	Emissivity	
	(<i>k</i>)	(ρ)	(<i>C</i>)	(ϵ)	
	W/m.K	kg/m³	J/kg.K	1st finish	2nd finish
Aluminum	167	2700	896	0.01-0.10	0.30-0.60
Stainless Steel	16.2	8000	500	0.01-0.15	0.20-0.60
Galvanized Steel	47.3	7850	475	0.15-0.45	

From the metal sheets, 20cmx20cm plates were cut and 5 cylindrical holes were drilled into each plate with an E-mill Acer EVS-3VKH to simulate defects. The defect pattern is shown in Figure 2-4 and the nominal dimensions for each defect are listed in Table 2.3.

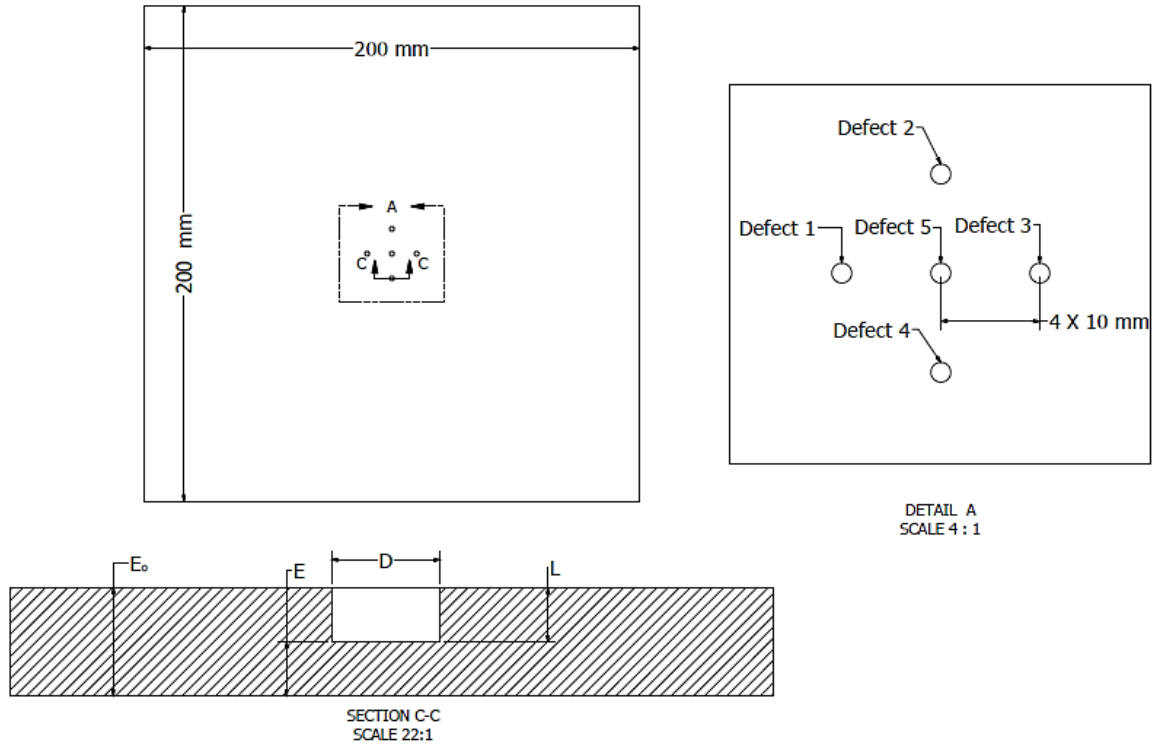


Figure 2-4 The defect plate arrangement.

Table 2.3 The nominal depth and diameter for each defect plate.

Plate	Defect 1		Defect 2		Defect 3		Defect 4		Defect 5	
	D (mm)	L (mm)	D (mm)	L (mm)	D (mm)	L (mm)	D (mm)	L (mm)	D (mm)	L (mm)
Array 1	1.00	1.00	1.00	0.50	1.00	0.25	1.00	0.75	1.00	0.10
Array 2	0.50	1.00	0.50	0.50	0.50	0.25	0.50	0.75	0.50	0.10
Array 3	1.50	0.25	1.00	0.25	0.50	0.25	2.00	0.25	0.25	0.25

After milling the defect depths were measured with a Brown and Sharpe 6 inch vernier caliper with an accuracy of $\pm 0.0253\text{mm}$. To measure diameter, microscopic images were taken of each defect with a Scalar DG-2A equipped with a 50x magnification lens to measure the defect diameter with a pixel size of $.003\text{mm}$. Two methods were used in the determination of the defect diameter. In the first method, points along the inner-edge of the defect were manually chosen and then fitted to a circle via the Taubin method[39, 40]. For this method, a minimum of

16 evenly spaced points were chosen, with more points used for larger defects. Figure 2-5 is the image of defect with a nominal size of 1.50mm in the mirror steel sheet with the fitted circle shown.

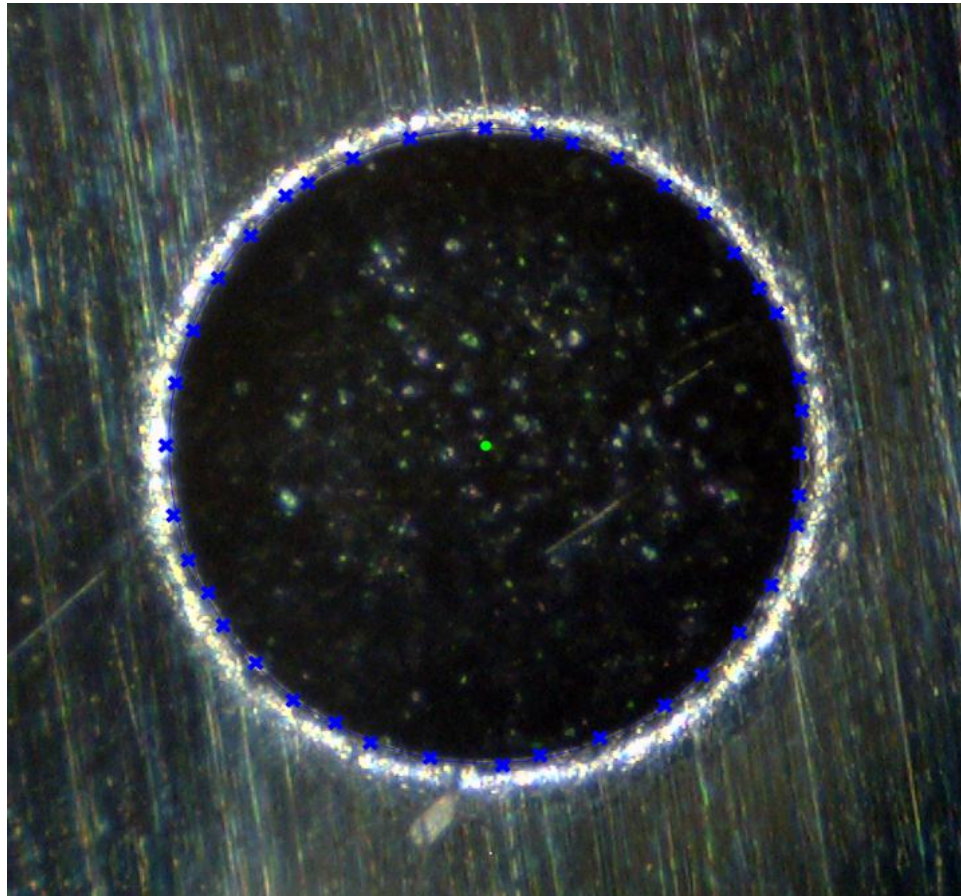


Figure 2-5 Circle Fitted to points chosen along the edge of the defect.

In the second method, the image of the defect is processed into a black and white image and the defect is then isolated from the surroundings and any gaps inside the defect image are filled in manually. This processes is demonstrated in Figure 2-6

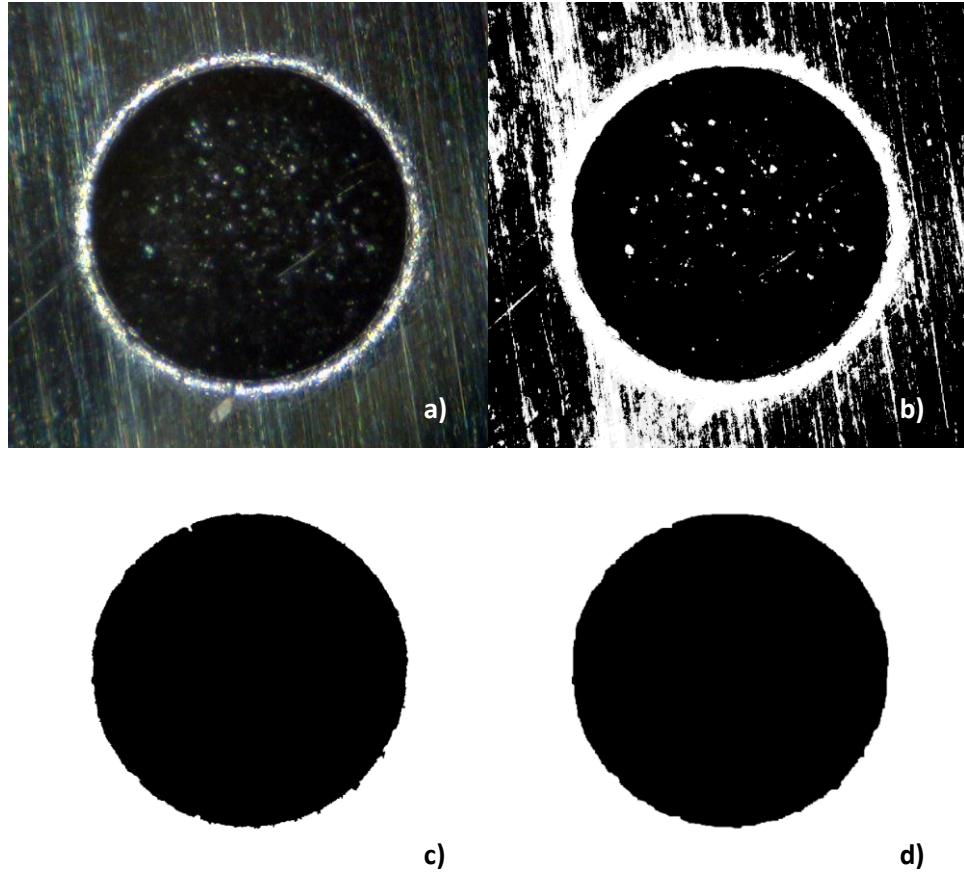


Figure 2-6 a) Microscopic image of defect in mirror finish steel sheet b) Processed black and white image c) Processed image with surroundings removed and holes filled in d) Errant pixels removed and morphological operations performed.

From Figure 2-6 d) the diameter of the defect is calculated in two ways. The pixels constituting the area of the defect are summed to find the area of the defect and from that area the diameter is determined assuming the defect is circular. Secondly, the edge pixels are fitted to a circle by the Taubin method. The results from both methods are averaged and compared to manually fitted circle for verification. The measured defect sizes can be found in Appendix A:.

iv. Estimation of Uncertainty

There are two major sources of error in the calculation of contrast, the heaters and the infrared detector. The SC4000 has an uncertainty of $\pm 2\%$ and the actual temperature has a greater error, but the difference (not the absolute value) is what is important. The black body heater has a spatial variation of 0.1 K and a temporal variation of 0.1 K, but the temporal variation is unimportant as 1 frame can be used for the calculation and that frame is captured in 2 ms or less. Examining the equation for contrast, S , in terms of temperature:

$$S = \frac{T_{px} - T_b}{T_b}$$

Where, T_b is the background temperature—for simplicity, the heater temperature—and T_{px} is the temperature represented by the pixel of interest. Thus the error in T_b is mainly caused by the heater's variability. The root sum square of these uncertainties is shown below.

$$S_{unc} = \sqrt{\left(\frac{\partial S}{\partial T_{px}} u_{T_{px}}\right)^2 + \left(\frac{\partial S}{\partial T_b} u_b\right)^2} = \sqrt{\left[\frac{1}{T_b} (T_{px} * .02)\right]^2 + \left[\frac{T_{px}}{T_b^2} (.1)\right]^2}$$

Considering the worst case scenario with $T_b = 303.15 \text{ K}$ and $T_{px} = T_{\infty} = 298.15 \text{ K}$:

$$S_{unc} \leq \sqrt{\left[\frac{1}{303.15} (298.15 * .02)\right]^2 + \left[\frac{298.15}{303.15^2} (.1)\right]^2} = .027$$

There is no data for the variability of the Ceramic heaters and while the error for them should be greater than that of the blackbody heaters it is unknown, but assumed to be of the same order of magnitude as the black body heaters.

v. Experimental Procedure

1. The sample holder is bolted to an optical table and then the distances for the heater and detector are measured and marked. The heater and camera are then placed in their respective spots.
2. The heater is turned on, set to the proper temperature or wattage and left to reach steady state for 1 hour.
3. A sample is placed in the holder and the camera is focused.
4. Samples to be inspected are then placed in the sample holder and data is recorded at 5 frames per second for one minute
5. Sample is removed and the recording is checked
6. Repeat steps 2-5 as needed.
7. Data is transferred into the MATLAB file format and defect centers are manually located.

Chapter Three: Results and Discussion

Contrast was used to determine the effect of each parameter tested. Contrast is how distinguishable an object is from its surroundings. However, contrast for an arbitrary image is not uniquely defined in literature [41]. In the case of a large, uniform background with a small test target, Weber contrast is commonly used [41]. The Weber contrast fraction is defined in Equation 3.1.

$$S = \left| \frac{I - I_b}{I_b} \right| \quad (3.1)$$

Where S is contrast, I is the intensity and I_b is the background intensity. In this case, the background intensity is the average temperature of a 10 px by 10 px sound area which is manually chosen. In the case of non-uniform background heating contrast is not well defined [41], but weber contrast will still be used in those cases. For the cases where contrast is calculated based on temperature the result is multiplied by 100 as dividing differences on the order of .5-10 K by values greater than 300K—this operation is not performed for contrasts of the Laplacian and gradient based thermograms.

i. Sample Images

Presented in this section are infrared images of each material and finish under different heating conditions.

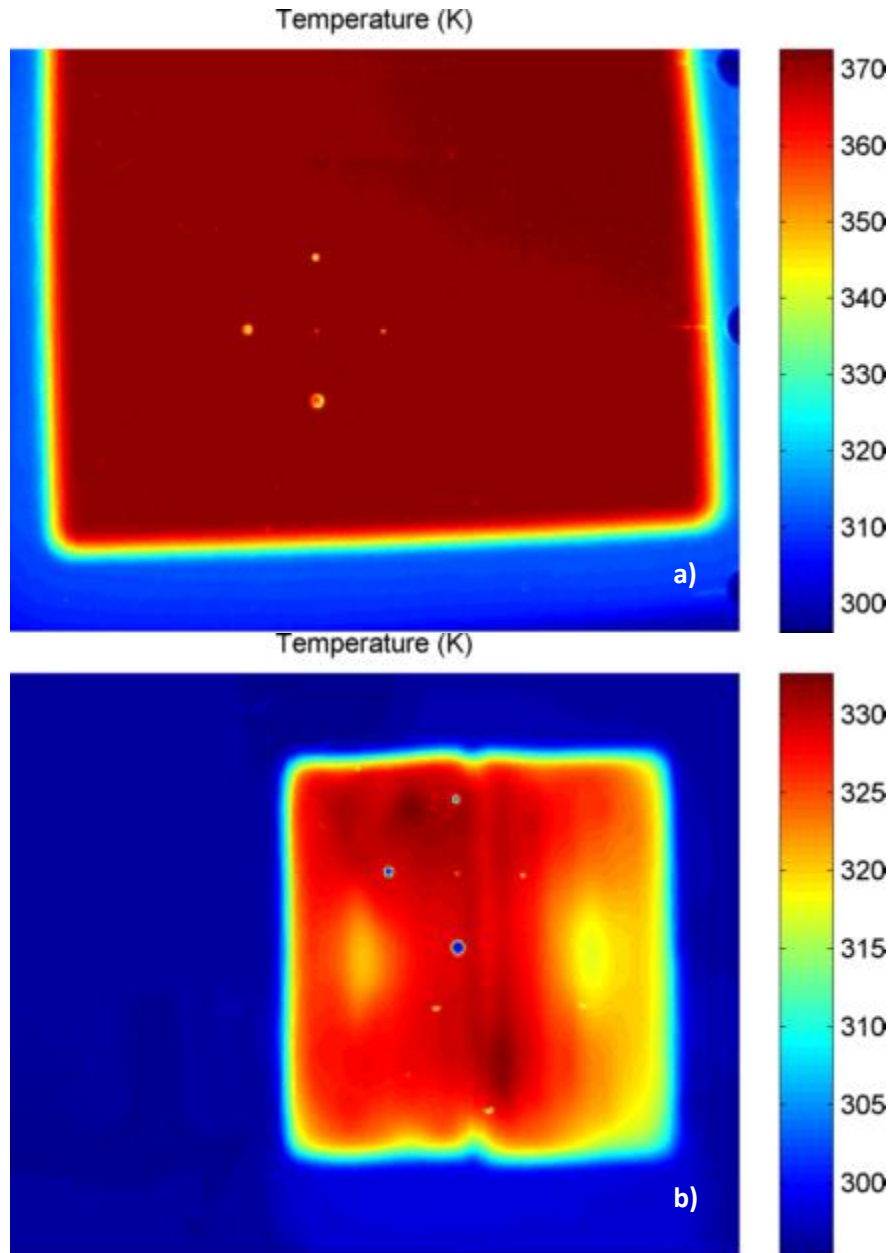


Figure 3-1 Array 3 of mirror-like finish Aluminum with a) black body heater at 373 K b) ceramic heater at 1093 W/m².

As shown in Figure 3-1, the black body heater provides even heating over its heating area, but the unevenness of the ceramic heater is quite pronounced for a low emissivity material such as mirror-like finish Aluminum alloy. In both cases the defects are visible. Processing may be able to mitigate the effect of the temperature variations in the ceramic heater.

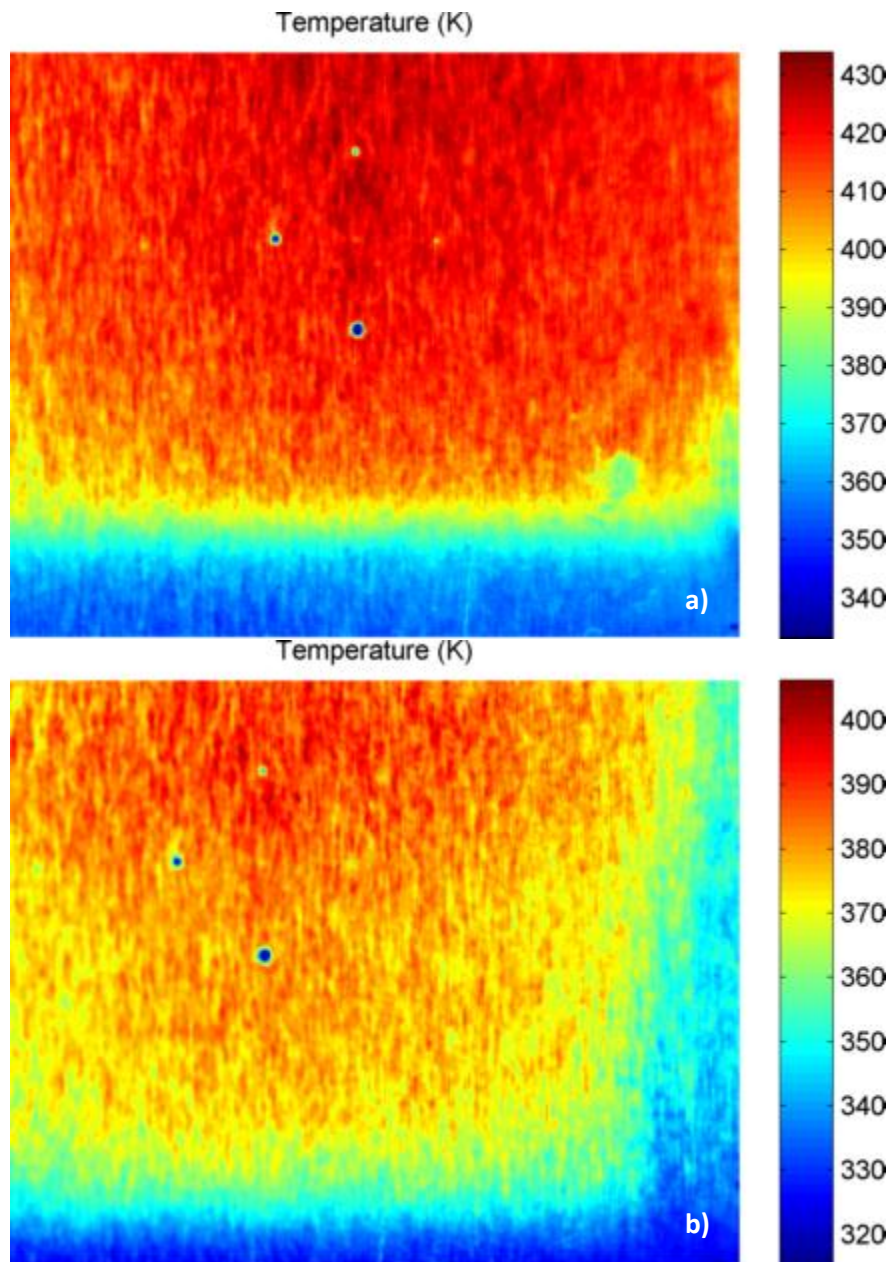


Figure 3-2 Array 3 of satin finish Aluminum with a) black body heater at 473 K b) ceramic heater at 1093 W/m².

The surface roughness of the satin finish aluminum samples is noticeable in Figure 3-2. The increased roughness and emissivity minimize the differences between the black body and ceramic heater. Only the larger defects are easily distinguishable; the diameter of the smallest defect, 0.281 mm, appears to be of the same order of magnitude as the width of the surface grooves.

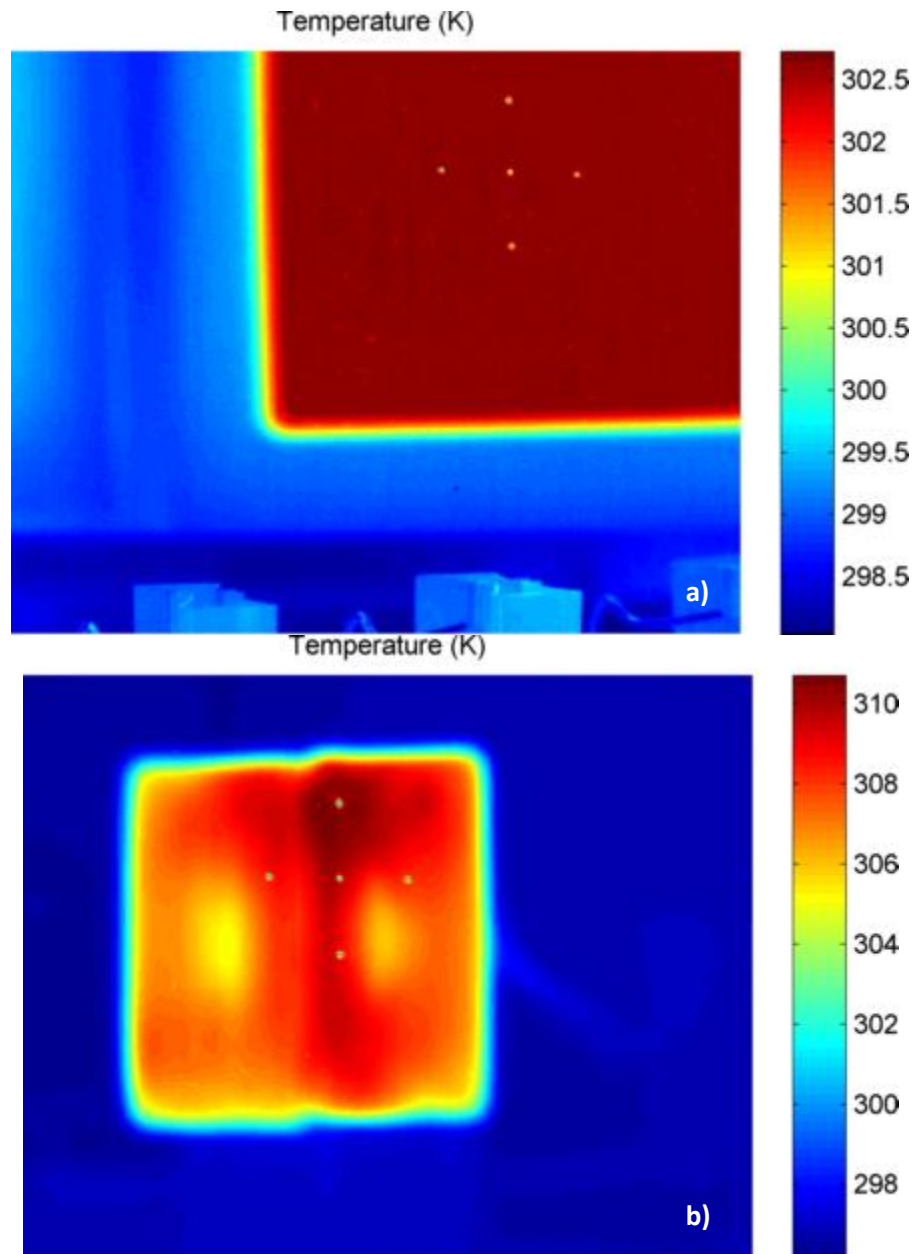


Figure 3-3 Array 2 of mirror-like finish stainless steel with a) black body heater at 303 K b) ceramic heater at 478 W/m².

The mirror-like finish stainless steel shown in Figure 3-3 appears very similar to that of the mirror-like finish Aluminum. Even with defects below the Nyquist frequency are visible on uniform and very low emissivity surfaces.

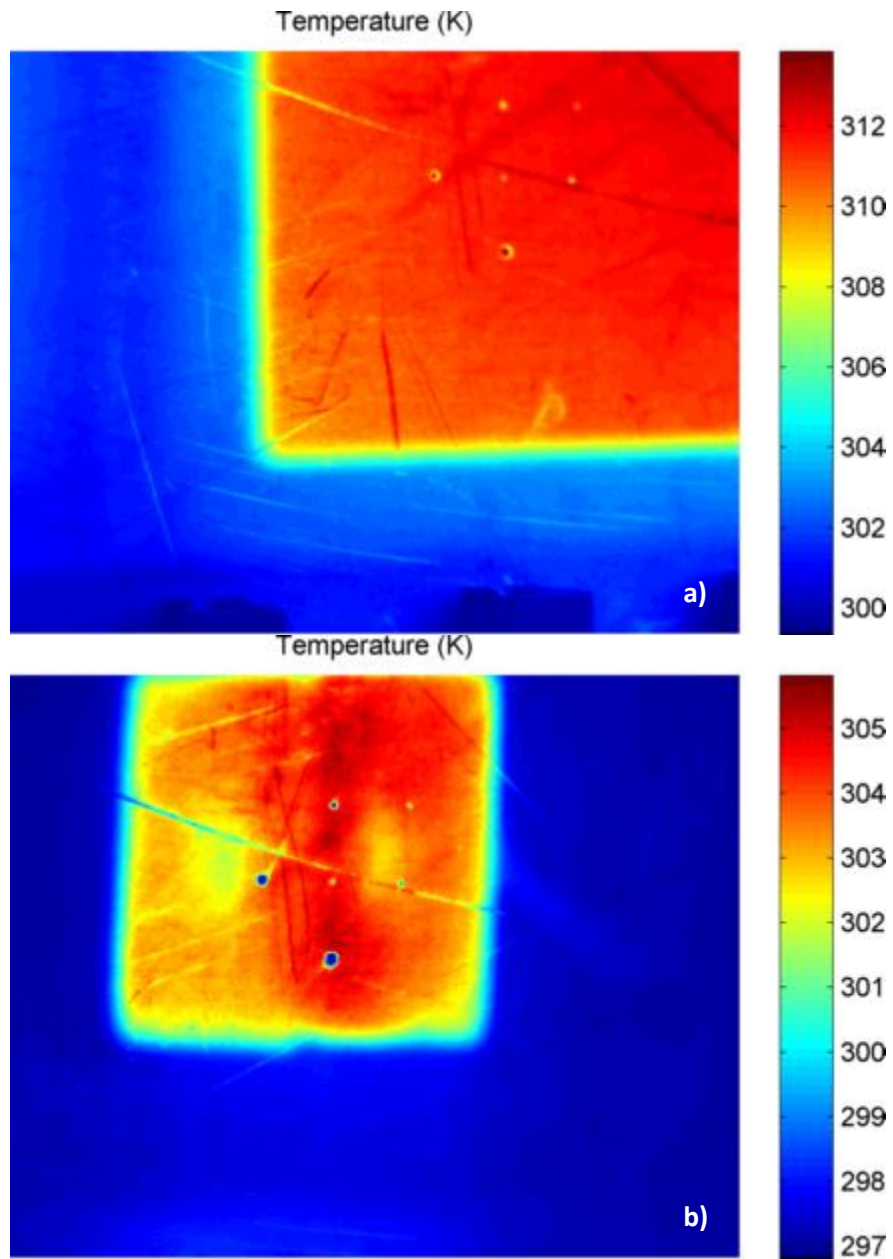


Figure 3-4 Array 3 of unpolished stainless steel with a) black body heater at 323 K b) ceramic heater at 615 W/m².

As shown in Figure 3-4, the unpolished steel is not uniform, with scratches and other markings. The defects in both are visible, but the 4th defect is very close to another discontinuity.

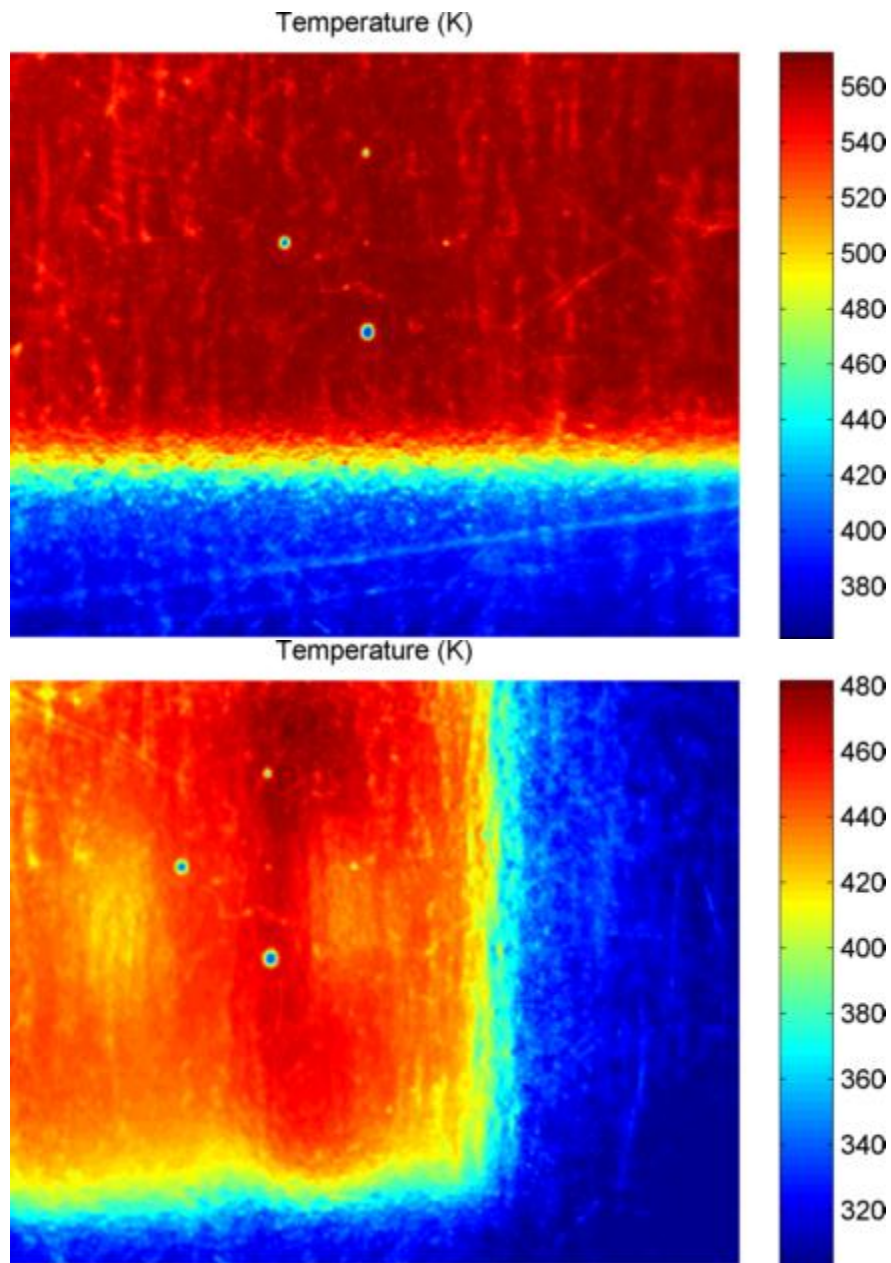


Figure 3-5 Temperature maps of Array 3 of galvanized steel with a) black body heater at 573 K b) ceramic heater at 6831 W/m².

The galvanized steel samples in Figure 3-5 show an uneven surface finish which may be due to variations in emissivity or the thickness of the Zinc coating.

ii. Effect of Diameter

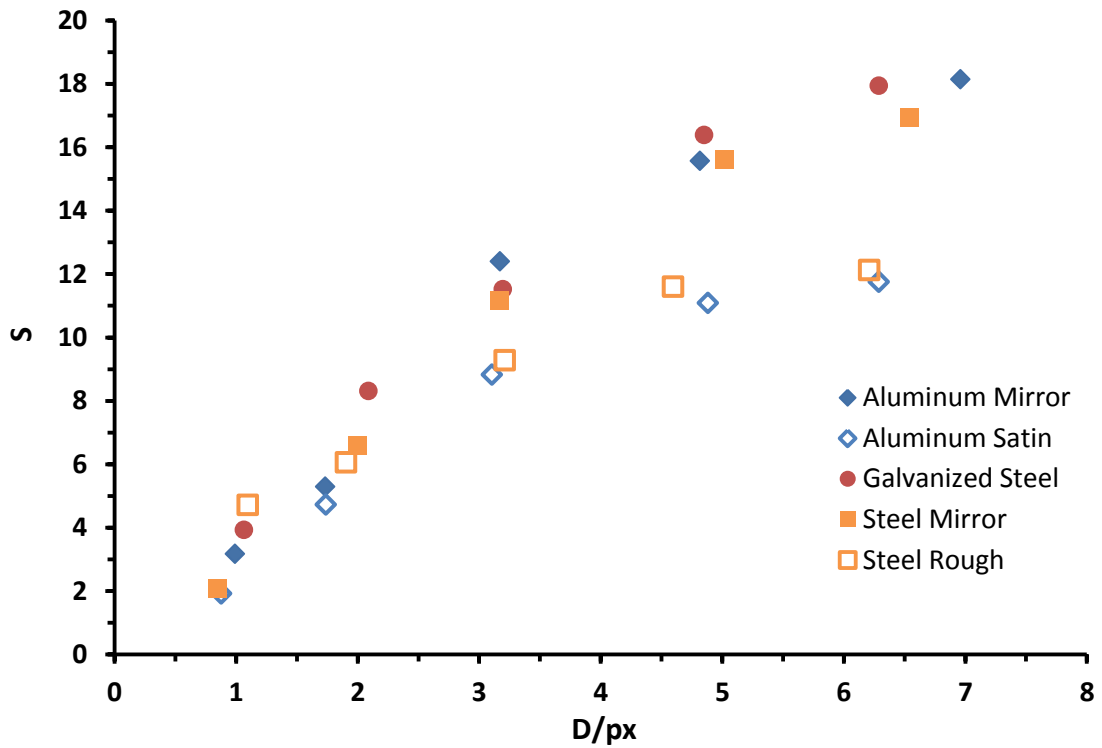


Figure 3-6 Diameter divided by pixel size plotted against contrast for array 3 with the black body heater at 373 K.

The effect of diameter appears to vary logarithmically with emissivity more so than material properties. To illustrate this, the Aluminum and Steel samples were plotted on a logarithmic scale in Figure 3-7.

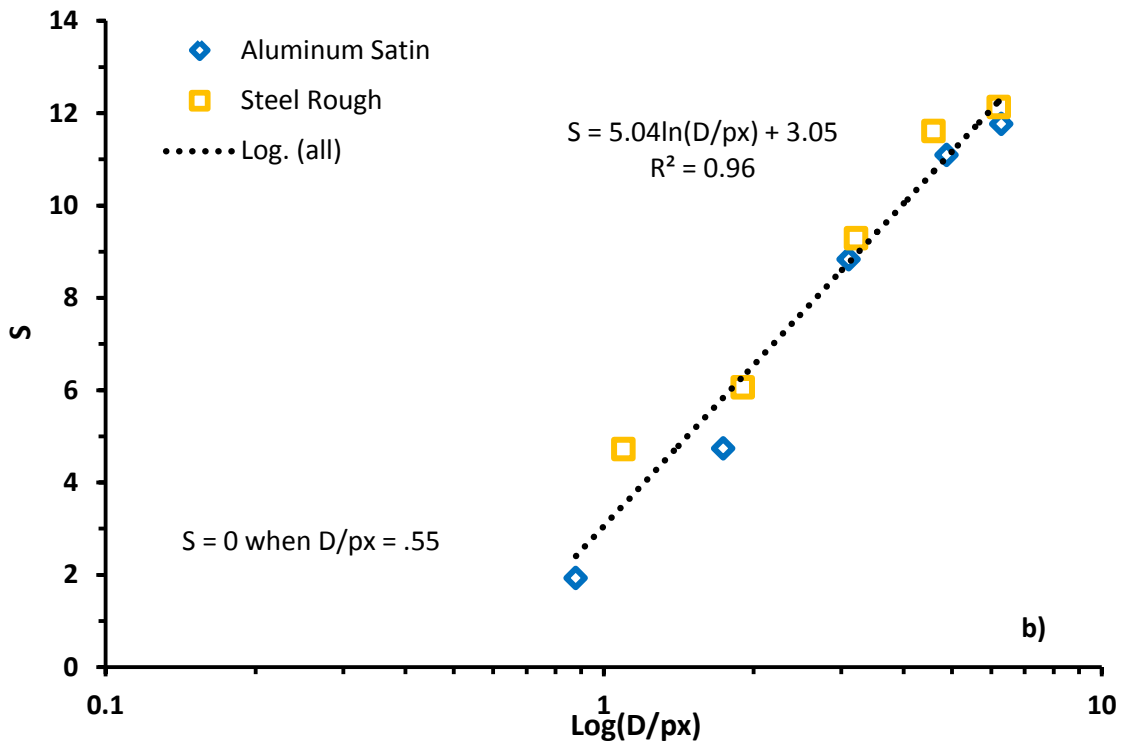
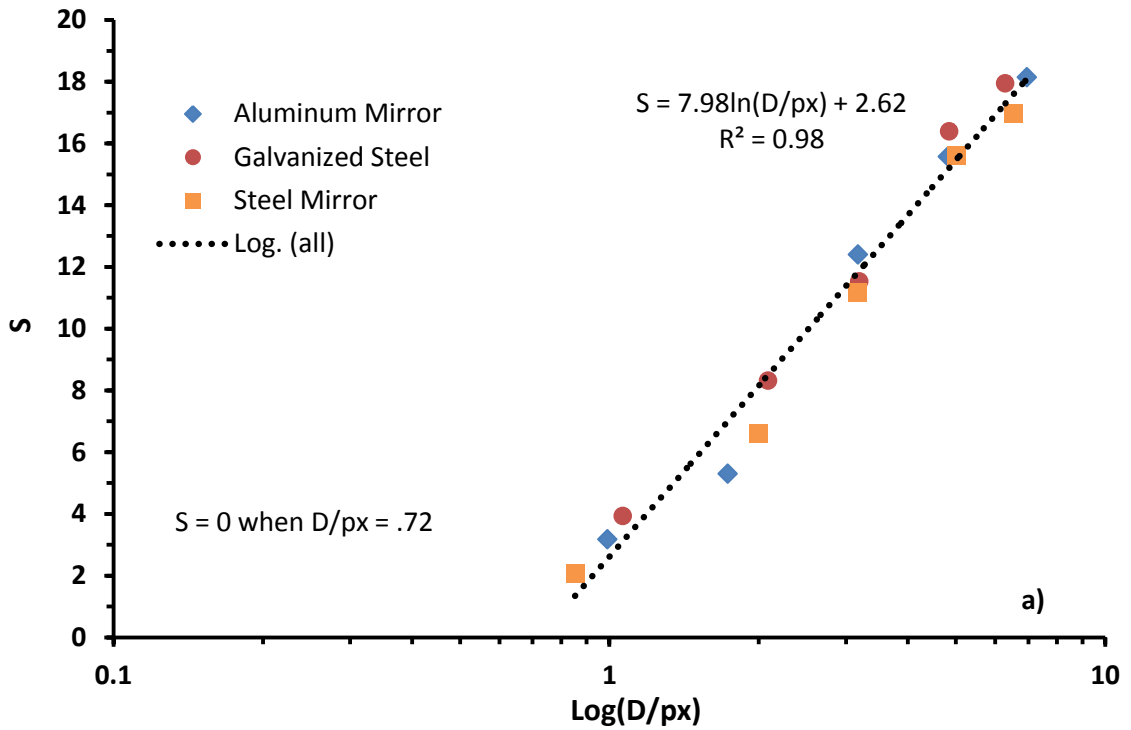


Figure 3-7 Effect of diameter for the array 3 with the black body heater at 373 K a) Low emissivity samples b) High emissivity samples.

The contrast appears to vary in a logarithmic manner and is dependent upon surface finish, not material properties. The change in contrast decreases as the diameter of the defect is represented by more pixels. In both cases, sub-pixel defects can be detected.

For defects that are uniform, the largest change is around the edge of the defect; having more pixels represent the interior of a large, uniform defect does not appear to provide a large increase in contrast. The pixels representing where the discontinuity begins show the largest change, while the uniform portion of the defect does not vary greatly as shown in Figure 3-8.

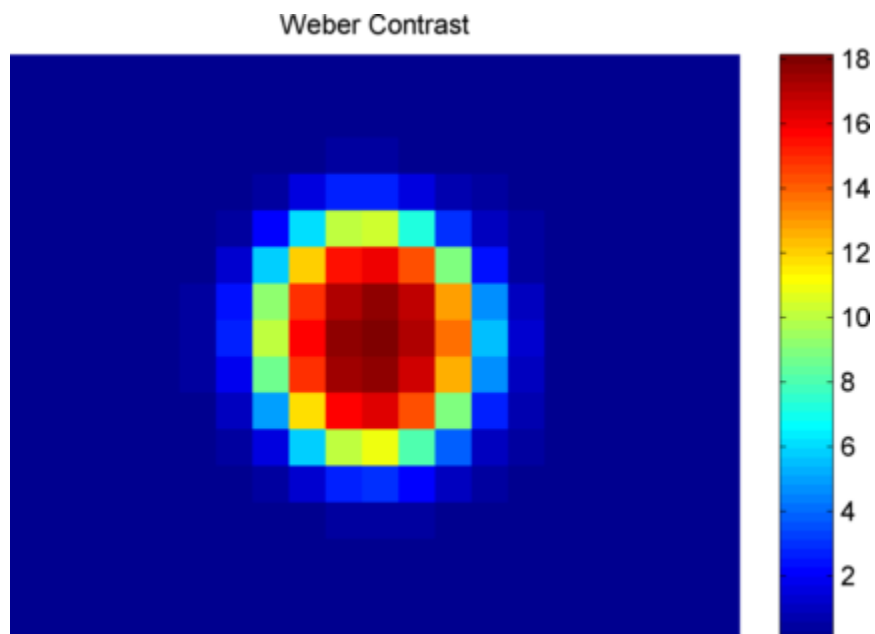


Figure 3-8 Contrast of a defect with D/px of 6.

iii. Detected Diameter

The diameter of each defect was determined via the same method used in the Sample Preparation section. The defect was isolated and edge detection was performed in MATLAB 2009a via the Sobel method with the default threshold. The area encompassed by the defect was then equated to the defect's diameter by assuming that it was circular.

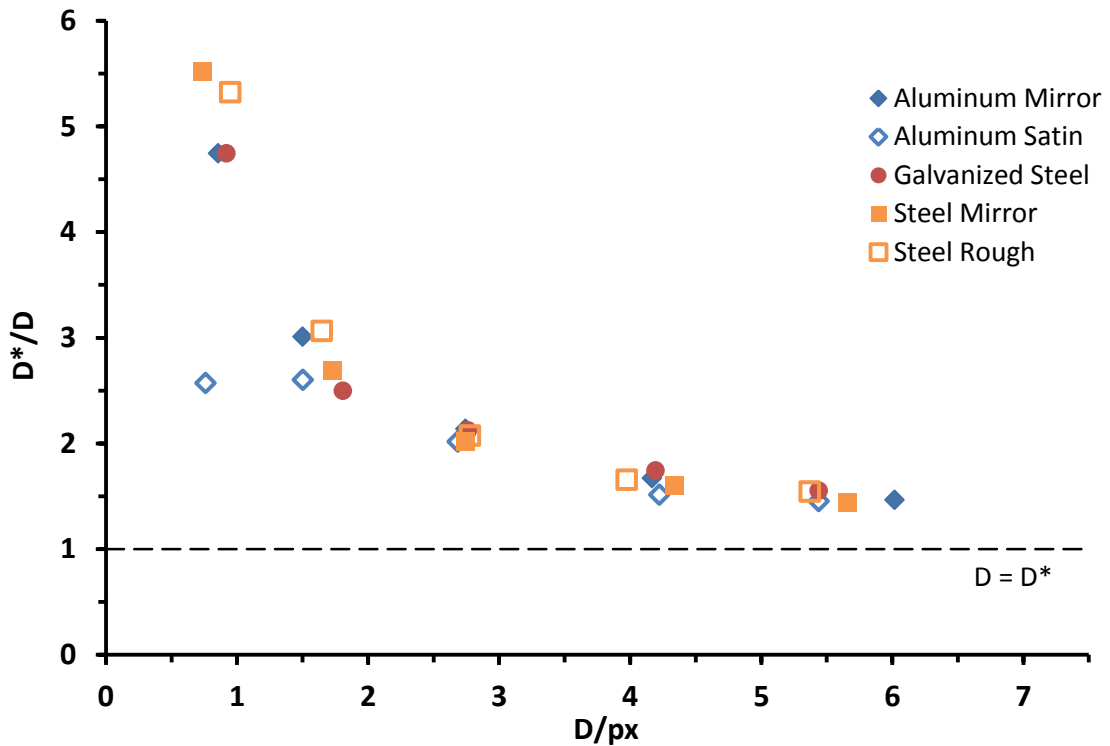


Figure 3-9 Detected diameter divided by the measured diameter plotted against the measured diameter over pixel size. Ceramic heater set to 478 W/m².

In Figure 3-9, the detected infrared diameter, D^* , is 30% greater than the measured diameter, D , at the highest diameter over pixel size and appears to be approaching one as there are more pixels comprise the defect.

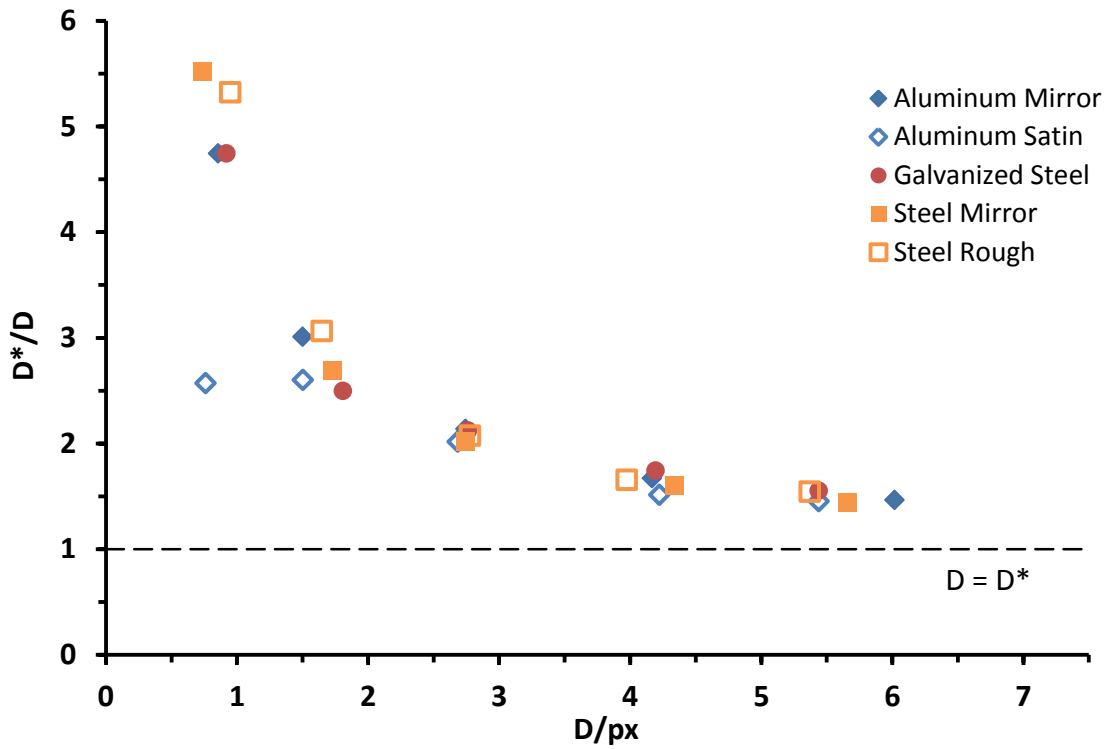


Figure 3-10 Detected diameter divided by the measured diameter plotted against the measured diameter over pixel size. Black body heater set to 573 K.

Figure 3-10 displays a similar trend to that of Figure 3-9, even with the tenfold increase in energy. As the number of pixels per defect increases the detected size approaches the measured size, while consistently staying above the measured size. The detected diameter is approximately 40% greater than the measure diameter at the largest D/px.

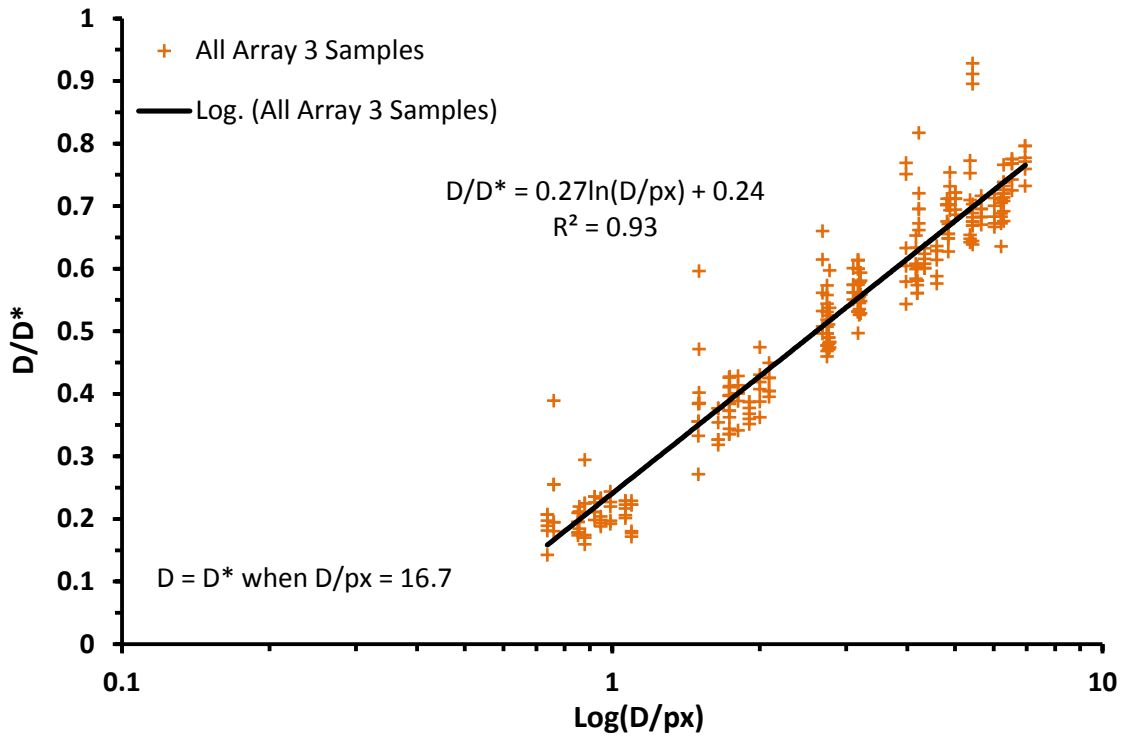


Figure 3-11 Measured diameter divided by the detected diameter and plotted against the measured diameter over pixel size for all array 3 tests.

Considering the data points from all of the tests in Figure 3-11, the detected diameter is 30-40% greater than that of the measured diameter. If the logarithmic trend holds the detected diameter will reach parity with the measured diameter when $D/\text{px} \approx 17$. This finding is congruent with a finding by Rantala et al. for the detection of cracks in ceramics via photothermal microscopy; the cracks were at least 34% longer than their optical measurement and the measurements were independent of modulation frequency [42]. Furthermore, the emission spectrum of the heater and the intensity does not appear to have a large effect on the detected diameter, nor does the material's thermal properties. Photothermal and infrared techniques may provide reliable crack length information in ceramics [26]. It requires some knowledge of the defect characteristics as it overestimates in a predictable manner. It appears that the infrared detector is capturing the effect of the defect on its surroundings.

iv. Effect of Aspect Ratio

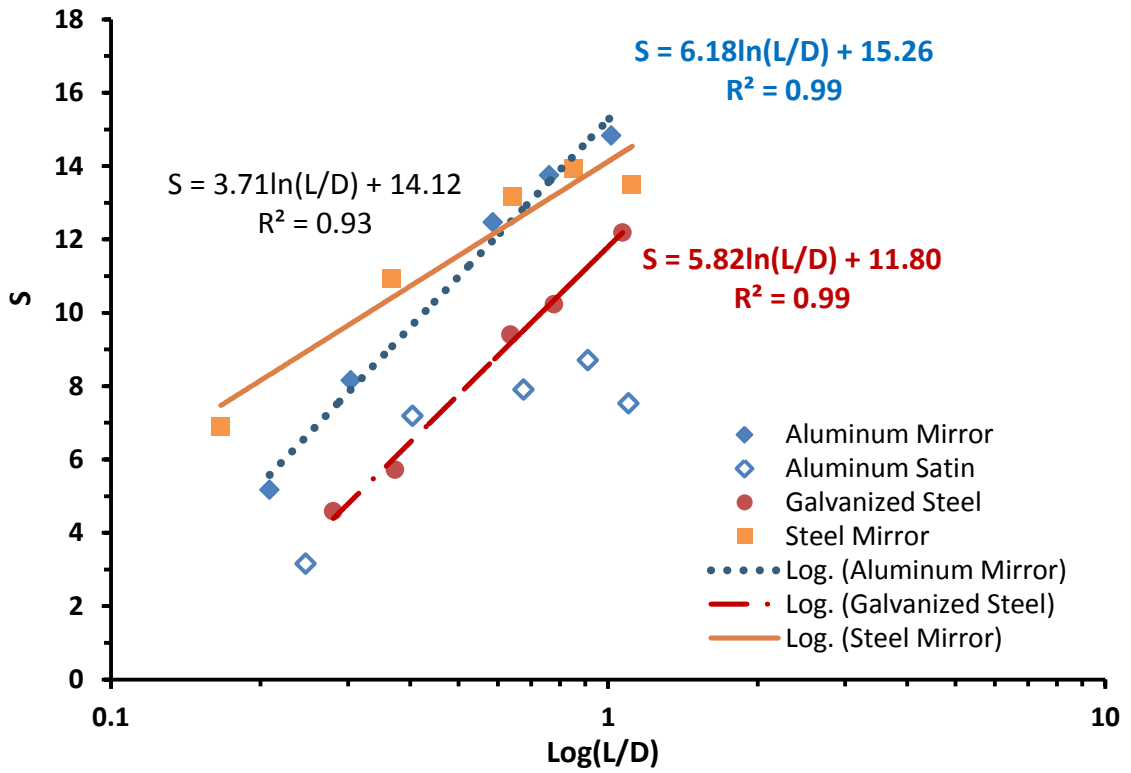


Figure 3-12 The effect of aspect ratio on contrast using data from array 1 with the black body heater at 373 K.

The effect of aspect ratio on contrast appears to be logarithmic for all samples in Figure 3-12 except the satin finish Aluminum which appears to follow no trend. The effect of aspect ratio is dependent upon the surface and material properties of the material and the defect. The detector is measuring the radiance from the defect walls. As the defect aspect ratio increases, less radiation from the bottom and the lower wall portions of the defect reaches the detector. Thus the surface characteristics of the defect are important as well.

v. Apparent Emissivity

The emissions from a cylindrical cavity may be characterized by the apparent emissivity, which gives the total energy leaving the opening of the cavity divided by that of the energy emitted by a black-walled cavity; which is the same as a black area the size of the cavity opening [37]. The effect of aspect ratio on the hemispherical equivalent emissivity is plotted in Figure 3-13.

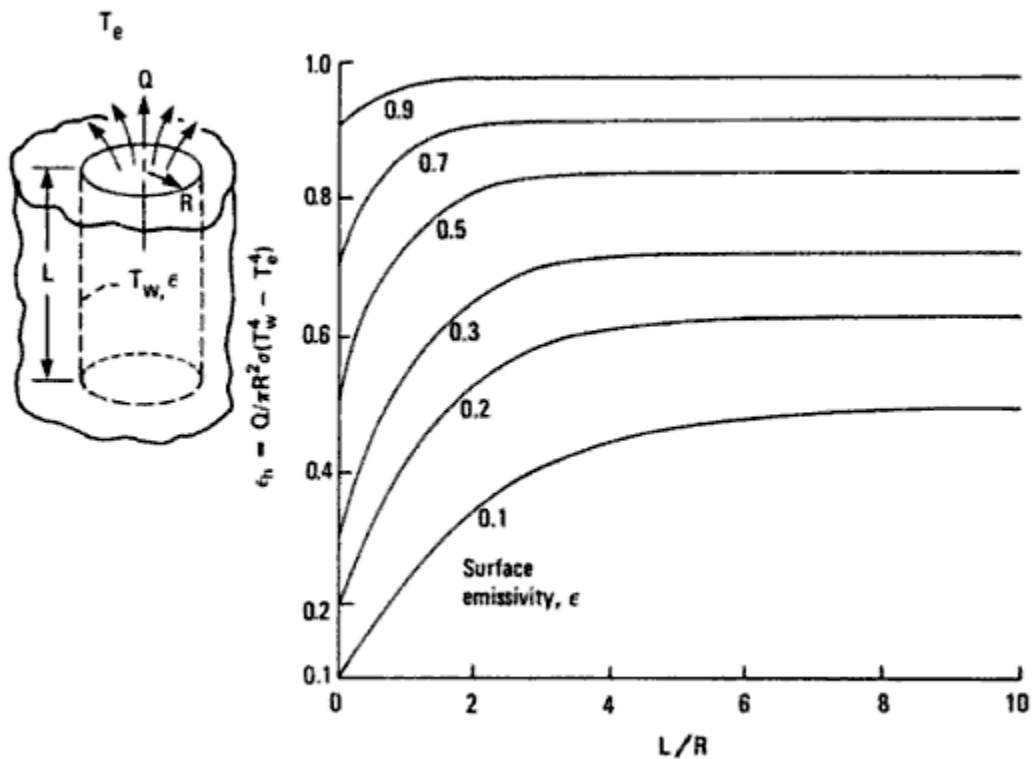


Figure 3-13 Apparent emissivity of a cavity opening for a cylindrical cavity of finite length with diffuse reflecting walls at a constant temperature. From Robert Siegel, John R. Howell; *Thermal Radiation Heat transfer*, 4th Edition [37].

To compare this information to the experimental data, the apparent emissivity, ϵ_a , of each defect and the surface emissivity, ϵ_s , was calculated assuming that the energy absorbed by the sample would be emitted thus $\epsilon = \kappa_s$ where κ_s is the surface absorptivity. Since the samples are

opaque $\varepsilon = 1 - \beta_s$ where β_s is the reflectivity. Thus $\varepsilon = 1 - \left| \frac{T_d^4 - T_\infty^4}{T_h^4 - T_\infty^4} \right|$, where T_d is the defect temperature, T_h is the heater temperature and T_∞ is the ambient temperature [37].

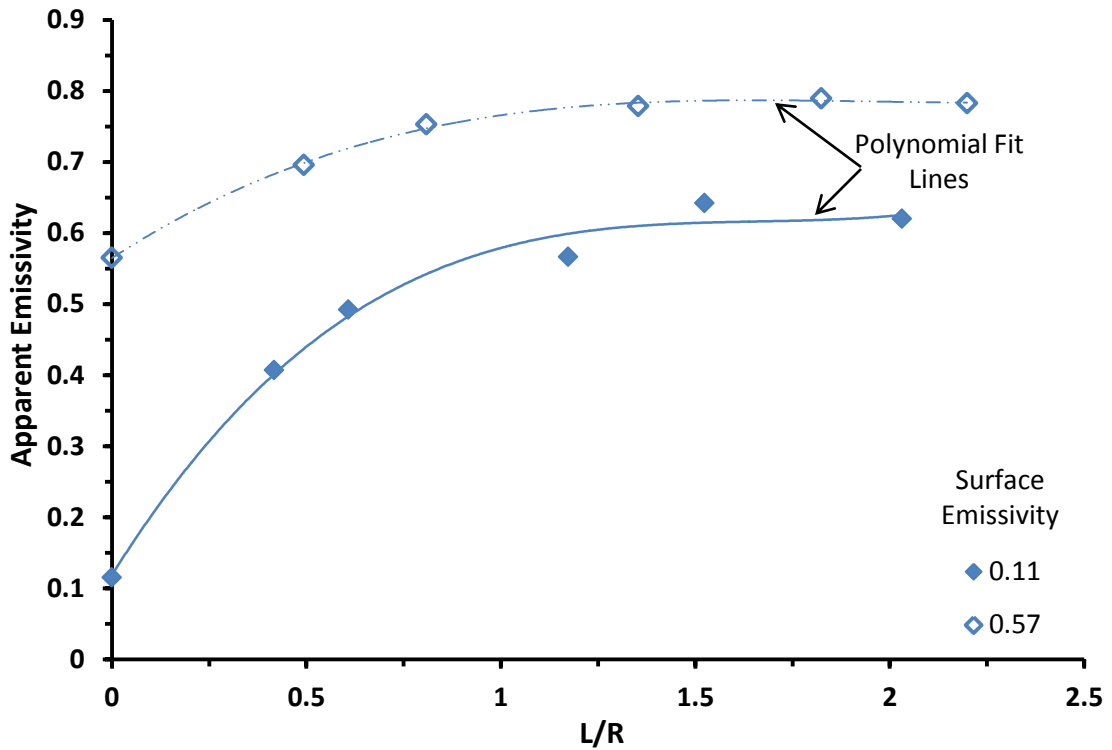


Figure 3-14 Apparent emissivity for the array 1 defects in the aluminum samples.

The trend from Figure 3-13 holds in Figure 3-14 even though the reflection—not the emission—from the samples is what is being measured as the samples are at ambient temperature. After a certain point, the change in aspect ratio has little to no effect on the apparent emissivity.

vi. Effect of Heating and Heaters

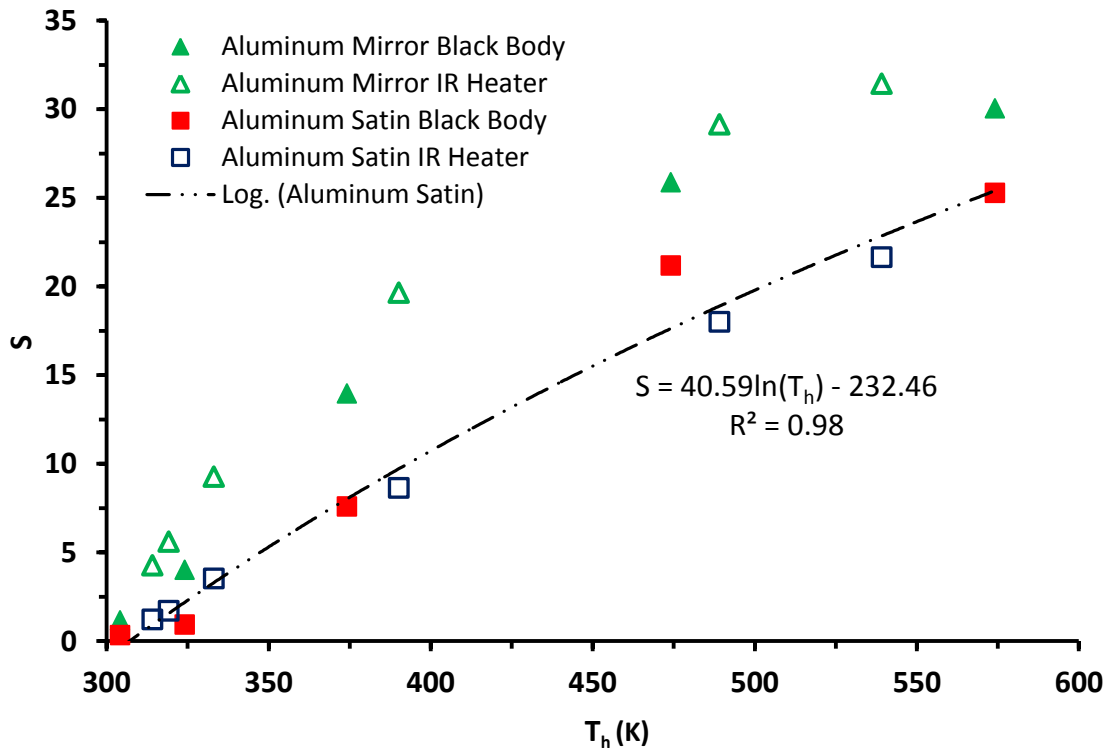


Figure 3-15 The effect of heating temperature on contrast by heater type on Aluminum samples with $D \approx 2\text{mm}$.

In Figure 3-15 the smoother mirror finish Aluminum the black body heater has a lower contrast in each case. This may be due to the variability of the heater or the difference in emission spectrums. The satin finish Aluminum does not exhibit the same behavior as both heaters are in the same general pattern with a very good curve fit for the combined data set. Instead of the temperature of the heater, consider the heat quality (HQ).

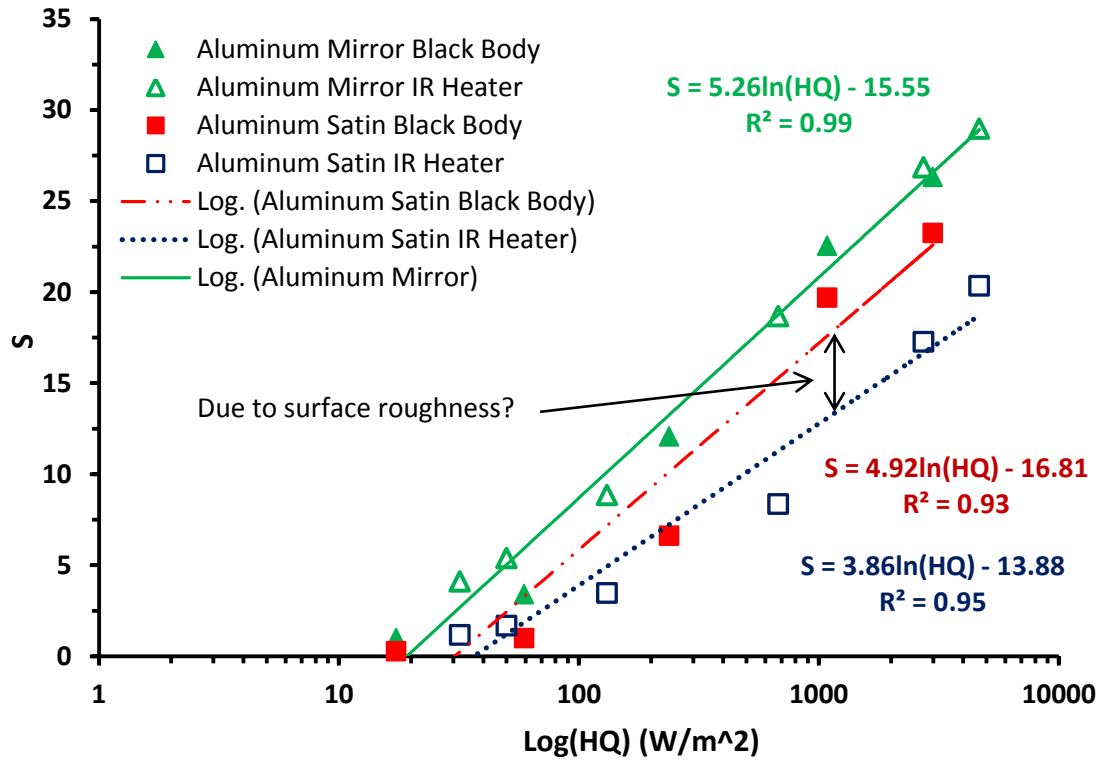
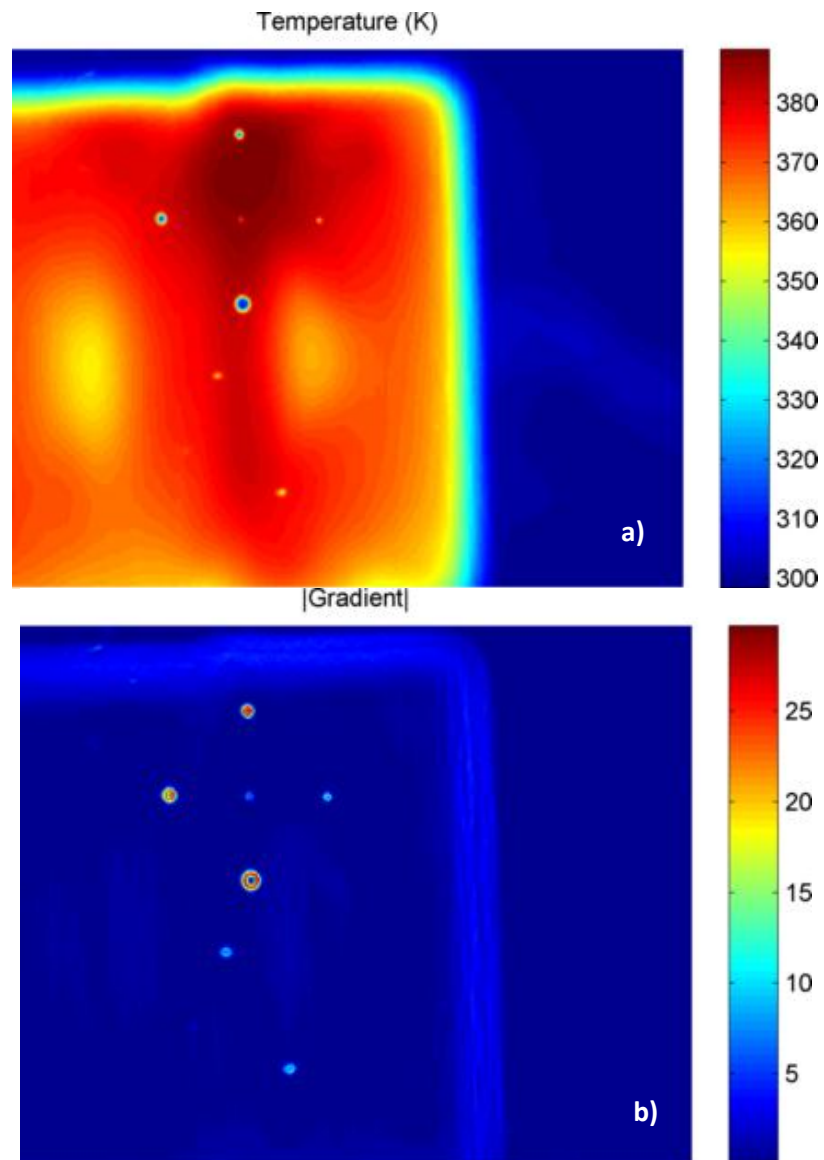


Figure 3-16 Effect of heat quality on contrast with respect to heater type.

In Figure 3-16, when HQ quality is on the abscissa the mirror-like sample converges while the rough sample diverges. The rough sample may interact differently with the longer wavelengths of the ceramic heater affecting the amount of absorption and scattering. It may be possible to use two heaters with different emission spectra to determine surface roughness with only one detection band for the detector.

vii. Derivatives as Filters

The gradient and Laplacian of the uniform area of a thermogram should be approximately zero as demonstrated in the mathematical formulation. Furthermore, small changes in heater uniformity should also be smoothed out as most heaters do not feature a sharp change in temperature within a small region.



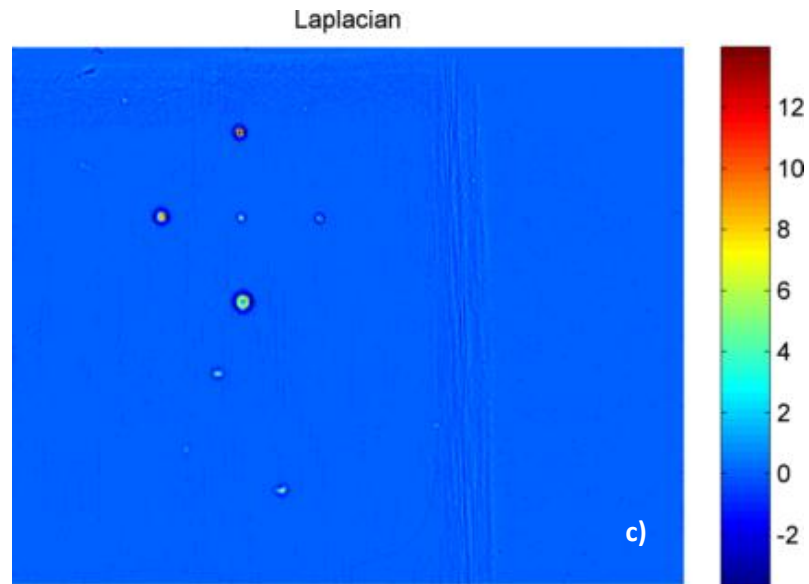


Figure 3-17 Aluminum Mirror Array 3 with ceramic heater at 2732 W/m^2 a) thermogram b) magnitude of the gradient of the thermogram c) Laplacian of the thermogram.

The derivatives images have a much higher signal for the defects than the surroundings as shown in Figure 3-17. The small variations in heater temperature are also mitigated. To demonstrate this contrast maps for the gradient and Laplacian were plotted in Figure 3-18. Note the sound area signal is approximately zero.

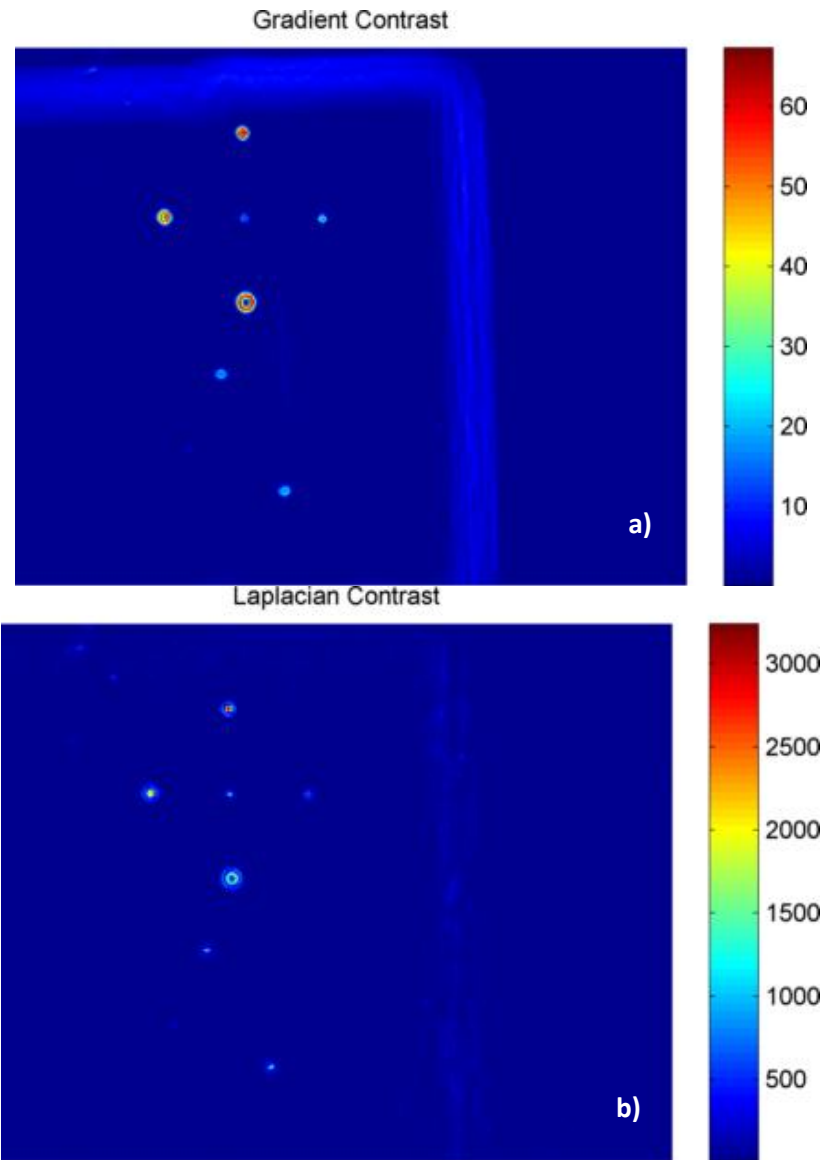


Figure 3-18 Contrast maps for a) gradient of temperature b) Laplacian of temperature.

The contrast for derivatives is much higher than that of the temperature contrast. It appears that the defect on the right is more easily detected by the gradient method, while the smallest defect in the center would be easier to detect by the Laplacian. Looking at the average contrast by material for all arrays and heating conditions in Figure 3-19

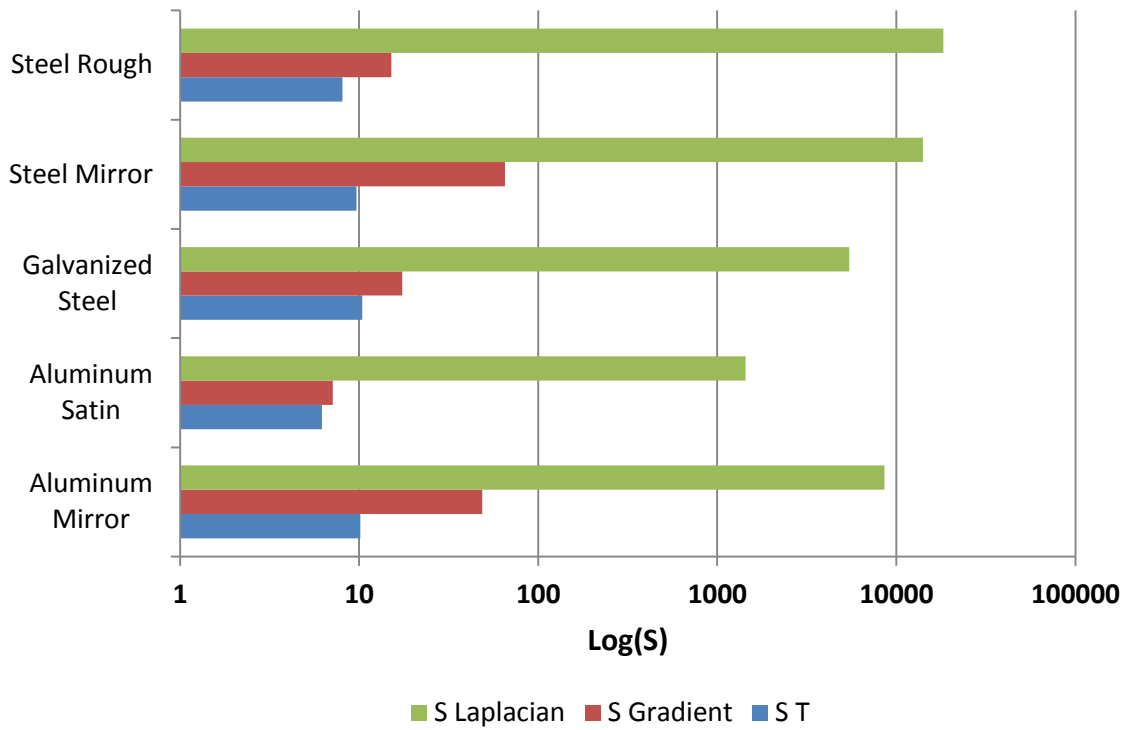


Figure 3-19 Average contrast by material for all defects, heating conditions and arrays.

The Laplacian contrast is always greater than the gradient contrast and both are always greater than the Temperature contrast. The temperature contrast is multiplied by 100 while the gradient and Laplacian contrasts are not.

Chapter Four: Conclusions and Future Work

Reflection mode IRT has been used to characterize cylindrical defects in metal sheets with varying defect sizes, surface finishes and material properties. The contrast of the defects is mainly governed by heat quality, the apparent surface emissivity and defect geometry. The temperature contrast follows a logarithmic trend in the cases shown.

It is possible to detect sub-pixel defects in some of the finishes. The mirror finishes and galvanized steel show better contrast in relation to D/px — even though the galvanized steel does not have a uniform surface finish—indicating that the contrast in relation to the defect diameter depends more on the apparent emissivity. Furthermore, this may also be due to the samples being specular or partially specular reflectors.

Regardless of surface finish, the detected diameter via infrared thermography is larger than the measured diameter. For all cases the measured diameter is at least 30% larger than the measured diameter. The detected diameter will reach parity measured diameter at a $D/px \approx 16$ if the trend holds. However, thermal effect of the defect on its surroundings should always cause the defect to appear larger than it is.

Derivatives can mitigate uneven heating and increase the contrast for defects even with rough surface finishes. The contrast for the gradient and Laplacian of temperature is always greater than that of the temperature contrast as the background intensity is approximately zero. The derivatives and thresholding can be used to detect defects and areas of interest.

In future work, I would like to attempt to measure surface roughness with two heaters of different wavelengths and one detector. Heat quality shows a large difference between heaters for the rough finish aluminum but not the mirror finish; the emissivity and surface roughness is suspected of being the cause.

Furthermore, study the same samples in transmission mode. Investigate different defect geometry and thermal property ratios; including defects with much larger diameters to verify the logarithmic trends seen and no change in geometry. Study the optical properties of semi-transparent media like plastics. Create a library allowing for the rapid deployment of IRT systems and possibly the automated detection of defects.

Appendix A: Defect Sizes

Compiled is a list of measurements for the depth and diameter of each defect.

Table A.1 Defect Measurements for Aluminum Mirror-Like Finish Samples.

Aluminum Mirror-Like Finish			
Array 1			
Defect	D (mm)	L (mm)	D/L
1	1.116	1.14	0.98
2	1.122	0.64	1.74
3	1.091	0.36	3.06
4	1.185	0.85	1.40
5	1.103	0.23	4.78

Array 2			
Defect	D (mm)	L (mm)	D/L
1	0.726	0.31	2.37
2	0.593	0.65	0.91
3	0.631	0.52	1.21
4	0.637	0.47	1.34
5	0.568	0.26	2.22

Array 3			
Defect	D (mm)	L (mm)	D/L
1	1.533	0.41	3.76
2	1.010	0.40	2.53
3	0.552	0.41	1.36
4	2.215	0.44	5.04
5	0.315	0.51	0.61

Table A.2 Defect Measurements for Aluminum Satin Finish Samples.

Aluminum Satin Finish			
Array 1			
Defect	D (mm)	L (mm)	D/L
1	1.082	1.19	0.91
2	1.064	0.72	1.48
3	1.064	0.43	2.45
4	1.064	0.97	1.10
5	1.014	0.25	4.11
Array 2			
Defect	D (mm)	L (mm)	D/L
1	0.588	1.09	0.54
2	0.576	0.56	1.03
3	0.582	0.30	1.93
4	0.588	0.81	0.73
5	0.594	0.57	1.04
Array 3			
Defect	D (mm)	L (mm)	D/L
1	1.563	0.42	3.69
2	0.994	0.42	2.34
3	0.556	0.48	1.15
4	2.013	0.44	4.60
5	0.281	0.30	0.95

Table A.3 Defect Measurements for Steel Mirror-Like Finish Samples.

Steel Mirror-Like Finish			
Array 1			
Defect	D (mm)	L (mm)	D/L
1	1.084	1.21	0.89
2	1.058	0.68	1.56
3	1.184	0.44	2.72
4	1.071	0.91	1.17
5	1.052	0.17	6.01
Array 2			
Defect	D (mm)	L (mm)	D/L
1	0.650	1.14	0.57
2	0.644	0.62	1.04
3	0.625	0.37	1.71
4	0.606	0.81	0.75
5	0.613	0.15	4.09
Array 3			
Defect	D (mm)	L (mm)	D/L
1	1.596	1.21	1.32
2	1.010	0.68	1.48
3	0.637	0.44	1.46
4	2.082	0.91	2.28
5	0.271	0.17	1.55

Table A.4 Defect Measurements for Steel Unpolished Finish Samples.

Steel Unpolished Finish			
Array 2			
Defect	D (mm)	L (mm)	D/L
1	0.654	1.02	0.44
2	0.635	0.56	1.14
3	0.559	0.30	1.89
4	0.616	0.54	1.13
5	0.578	0.12	4.63
Array 3			
Defect	D (mm)	L (mm)	D/L
1	1.47	0.28	5.32
2	1.03	0.29	3.52
3	0.61	0.29	2.09
4	1.99	0.27	7.46
5	0.35	0.19	1.88

Table A.5 Defect Measurements for Galvanized Steel Samples.

Galvanized Steel			
Array 1			
Defect	D (mm)	L (mm)	D/L
1	1.164	1.24	0.93
2	1.113	0.71	1.57
3	1.069	0.40	2.68
4	1.176	0.92	1.28
5	1.063	0.30	3.57
Array 2			
Defect	D (mm)	L (mm)	D/L
1	0.662	1.04	0.64
2	0.669	0.59	1.13
3	0.669	0.30	2.21
4	0.638	0.83	0.77
5	0.619	0.15	4.14
Array 3			
Defect	D (mm)	L (mm)	D/L
1	1.552	0.43	3.58
2	1.022	0.42	2.41
3	0.669	0.42	1.58
4	2.013	0.44	4.58
5	0.341	0.37	0.91

References

1. Maldague, X.P.V., *Nondestructive Testing Handbook*. 3 ed, ed. P.O. Moore. Vol. 3. 2001: American Society for Nondestructive Testing.
2. Frauenthal, A.H., *Ten Year's Progress in Inspection*. Manufacturing Industries, 1928: p. 99-102.
3. Shingō, S., *A study of the Toyota production system from an industrial engineering viewpoint*. 1989: Productivity Press.
4. Maldague, X.P.V., *Theory and Practice of Infrared Technology for Nondestructive Testing*. 1 ed. 2001: Wiley-Interscience.
5. Smid, R., A. Docekal, and M. Kreidl, *Automated classification of eddy current signatures during manual inspection*. NDT & E International, 2005. **38**(6): p. 462-470.
6. Cielo, P.G. *On-line optical sensors for industrial material inspection*. 1990. The Hague, Netherlands: SPIE.
7. DuPont, F., C. Odet, and M. Cartont, *Optimization of the recognition of defects in flat steel products with the cost matrices theory*. NDT & E International, 1997. **30**(1): p. 3-10.
8. Morishita, I. and M. Okumura, *Automated visual inspection systems for industrial applications*. Measurement. **1**(2): p. 59-67.
9. Sophian, A., et al., *A feature extraction technique based on principal component analysis for pulsed Eddy current NDT*. NDT & E International, 2003. **36**(1): p. 37-41.
10. Tian, G.Y. and A. Sophian, *Defect classification using a new feature for pulsed eddy current sensors*. NDT & E International, 2005. **38**(1): p. 77-82.
11. *Ultrasonic monitoring of texture in cold-rolled steel sheets: Hirao, M.; Hara, N.; Fukuoka, H.; Fujisawa, K. Journal of the Acoustical Society of America, vol. 84, no. 2, pp. 667-672 (Aug. 1988)*. NDT International, 1989. **22**(5): p. 306-306.
12. Hassan, M., O. Burdet, and R. Favre, *Ultrasonic measurements and static load tests in bridge evaluation*. NDT & E International, 1995. **28**(6): p. 331-337.
13. Mozurkewich, G., B. Ghaffari, and T.J. Potter, *Spatially resolved ultrasonic attenuation in resistance spot welds: Implications for nondestructive testing*. Ultrasonics, 2008. **48**(5): p. 343-350.
14. Omar, M.A., et al., *Infrared thermography (IRT) and ultraviolet fluorescence (UVF) for the nondestructive evaluation of ballast tanks' coated surfaces*. NDT & E International, 2007. **40**(1): p. 62-70.
15. Omar, M., et al., *IR self-referencing thermography for detection of in-depth defects*. Infrared Physics & Technology, 2005. **46**(4): p. 283-289.
16. Astarita, T., et al., *A survey on infrared thermography for convective heat transfer measurements*. Optics & Laser Technology, 2000. **32**(7-8): p. 593-610.
17. Bormashenko, E., et al., *Optical properties and infrared optics applications of composite films based on polyethylene and low-melting-point chalcogenide glass*. Optical Engineering, 2002. **41**(2): p. 295-302.
18. Varis, J., J. Rantala, and J. Hartikainen, *An infrared line scanning technique for detecting delaminations in carbon fibre tubes*. NDT & E International, 1996. **29**(6): p. 371-377.
19. Madruga, F.J., et al., *Infrared thermography processing based on higher-order statistics*. NDT & E International. **In Press, Accepted Manuscript**.
20. Darabi, A. and X. Maldague, *Neural network based defect detection and depth estimation in TNDE*. NDT & E International, 2002. **35**(3): p. 165-175.
21. Krishnapillai, M., et al., *Thermography as a tool for damage assessment*. Composite Structures, 2005. **67**(2): p. 149-155.

22. Badghaish, A.A. and D.C. Fleming, *Non-destructive Inspection of Composites Using Step Heating Thermography*. Journal of Composite Materials, 2008. **42**(13): p. 1337-1358.
23. Omar, M.A., R. Parvataneni, and Y. Zhou, *A combined approach of self-referencing and Principle Component Thermography for transient, steady, and selective heating scenarios*. Infrared Physics & Technology. **In Press, Corrected Proof**.
24. McCrea, A., D. Chamberlain, and R. Navon, *Automated inspection and restoration of steel bridges--a critical review of methods and enabling technologies*. Automation in Construction, 2002. **11**(4): p. 351-373.
25. Duisburg-Essen, U.o., *Solid Ceramic Emitters*. 2010, Frieder Freek. p. Spectral Emission of a Solid Ceramic Heater.
26. Muratikov, K., et al., *Photodeflection and photoacoustic microscopy of cracks and residual stresses induced by Vickers indentation in silicon nitride ceramic*. Technical Physics Letters, 1997. **23**(3): p. 188-190.
27. Maierhofer, C., R. Arndt, and M. Röllig, *Influence of concrete properties on the detection of voids with impulse-thermography*. Infrared Physics & Technology, 2007. **49**(3): p. 213-217.
28. Maierhofer, C., et al., *Application of impulse-thermography for non-destructive assessment of concrete structures*. Cement and Concrete Composites, 2006. **28**(4): p. 393-401.
29. Colak, A., et al., *Short Communication: Early Detection of Mastitis Using Infrared Thermography in Dairy Cows*. Journal of Dairy Science, 2008. **91**(11): p. 4244-4248.
30. FLIR. *ThermoVision® SC4000*. 2008; Available from: www.flir.com/WorkArea/linkit.aspx?LinkIdentifier=id&ItemID=19970.
31. *IR-160/301 Blackbody System*. [cited 2010 November 4, 2010]; Available from: <http://www.infraredsystems.com/Products/blackbody160.html>.
32. *IR-301 Controller*. [cited 2010 November 4]; Available from: <http://www.infraredsystems.com/Products/ir301.html>.
33. Kane, R. and H. Sell, *Revolution in Lamps : A Chronicle of 50 Years of Progress*. 2001, The Fairmont Press: Lilburn, GA.
34. *HTE (Half Trough Emitter)*, cerami29.gif, Editor, MOR Electric Heating.
35. Rammohan Rao, V. and V.M.K. Sastri, *Efficient evaluation of diffuse view factors for radiation*. International Journal of Heat and Mass Transfer, 1996. **39**(6): p. 1281-1286.
36. Lauzier, N. and D. Rouse, *View Factors with GUI*. 2005.
37. Siegel, R. and J. Howell, *Thermal Radiation Heat Transfer*. 4 ed. 2001: Taylor & Francis.
38. Incropera, F.P., DeWitt, D. P., *Introduction to Heat Transfer*. 5 ed. 2007: John Wiley & SONS, Inc.
39. Al-Sharadqah, A. and N. Chernov, *Error analysis for circle fitting algorithms* Electronic Journal of Statistics, 2009. **3**: p. 886-911 (electronic).
40. Chernov, N., *Circle Fit (Taubin method)*. 2009.
41. Peli, E., *Contrast in complex images*. J. Opt. Soc. Am. A, 1990. **7**(10): p. 2032-2040.
42. Rantala, J., J. Hartikainen, and J. Jaarinen, *Photothermal determination of vertical crack lengths in silicon nitride*. Applied Physics A: Materials Science & Processing, 1990. **50**(5): p. 465-471.

Vita

Marc Anthony Harik

Born: October 16, 1987 in Lexington, Kentucky

Educational Institutions

- Tates Creek High School, Lexington, KY, August 2000 – May 2005, Commonwealth Diploma May, 2005
- University of Kentucky, Lexington, KY, College of Engineering, Mechanical Engineering, August 2005 – May 2009

Professional Positions

May 2009 - Tennessee Valley Authority Fellow, Institute of Research for Technology Development, Lexington, KY

May 2006 – May 2009 Bucks for Brains Fellow, University of Kentucky, Lexington, KY

Scholastic/Professional Honors

- UK Engineering Alumni Association; Secretary 2009-2011
- Engineering Student Council; President 2009-2010
- American Society of Mechanical Engineering @ UK; President, VP 2007-2009
- Nagoya University Summer Intensive Program; Participant 2010
- US Department of Energy Solar Decathlon; Decathlete 2008-2009
- AIAA Design-Build-Fly Competition; Participant 2008-2009
- International Karakuri Workshop; Participant 2007